https://doi.org/10.5194/egusphere-2026-2705
Preprint. Discussion started: 8 July 2026

Evaluation and Correction of Precipitation Types Measured by a PARSIVEL2 Disdrometer in a Tropical Glacier Environment

María A. Pérez-Tello[1,3*], Iralmy Platero[1], Jairo M. Valdivia[2], Daniel Martinez-Castro[3], Elver E. Villalobos-Puma[4], and Fey Y. Silva[3]

[1]Facultad de Ingeniería, Escuela Académica Ambiental, Universidad Continental, Huancayo, Junín, Perú
[2]Department of Atmospheric and Oceanic Sciences, University of Colorado Boulder, Boulder, Colorado, USA
[3]Subdirección de Ciencias de la Atmosfera e Hidrósfera, Instituto Geofísico del Perú (IGP), Lima, Perú
[4]Instituto Nacional de Investigación en Glaciares y Ecosistemas de Montaña, INAIGEM, Huaraz, 100190, Ancash, Perú

Correspondence: María A. Pérez-Tello (mariapereztello29@gmail.com)

Abstract.

Precipitation characteristics in high-mountain regions with complex terrain remain poorly understood because observational networks are sparse and robust instrumentation is rarely deployed. This study evaluates precipitation type measurements from a PARSIVEL2 optical disdrometer installed at 4709 m a.s.l., approximately 2.5 km from the Huaytapallana tropical glacier system in the Peruvian Andes. The instrument measures the equivalent diameter and fall velocity from particle shadows crossing its laser beam; it then computes precipitation intensity (mm h^{-1}) and classifies hydrometeor types at 1 min resolution. Based on one year of observations, we identified seven precipitation types: rain, drizzle, drizzle with rain, snow, hail, soft hail, and mixed rain drizzle with snow. The original PARSIVEL2 classification indicated that drizzle with rain was the most frequent type (30.57%), followed by snow (26.15%). We identified 70 precipitation events (duration $\geq$10 min) and compared the corresponding accumulations against a Pluvio2 weighing rain gauge (threshold $\geq$0.25 mm). The PARSIVEL2 systematically overestimated precipitation, especially during mixed-phase events (98.5%, 3.92 mm bias) and solid precipitation events (84.1%, 7.09 mm bias), whereas liquid precipitation events showed minimal bias (15.7%, 0 mm bias). The largest discrepancies occurred during extreme events (>10.6 mm and >1 h) dominated by snow, soft hail, and hail, which we attribute to misclassification of coexisting particle types and systematic deviation of the instrument's internally calculated density values. We developed a correction methodology that combines velocity–diameter reclassification criteria based on established empirical relationships with site specific density optimization. For solid precipitation, RMSE decreased from 13.05 to 4.4 mm; for mixed precipitation, the scope value improved from 1.936 to 1.004. The corrected classification identified wet snow (29.3%) and graupel (15%) as dominant precipitation types, whereas pure snow represented only 3.7% . These results demonstrate the need for post processing corrections of disdrometer measurements in tropical glacier environments and provide an improved characterization of mixed-phase precipitation processes relevant to glacier mass balance assessments.

1 Introduction

Concerns about water availability have been linked to declining glacier cover in tropical regions (Buytaert et al., 2017). Recent studies also indicate that groundwater is the main source of water during the dry season. Approximately 2% of groundwater recharge comes from glacier melt, whereas precipitation can be very high in mountainous regions (Somers et al., 2019). The regional environment is characterized by complex orographic patterns (Villalobos-Puma et al., 2024) and diverse precipitation types (Llactayo et al., 2024). However, misclassification of precipitation types by disdrometers can bias estimated precipitation amounts.

Precise precipitation quantification is essential for hydrological applications, climate modeling, and weather forecasting. However, accurate measurement and characterization remain challenging, particularly for solid precipitation such as snow and hail (Boudala et al., 2014; Thériault et al., 2021). Despite instrument limitations, disdrometers substantially improve our understanding of precipitation characteristics. Optical disdrometers have been widely used since the 1990s because they provide high-temporal-resolution measurements of hydrometeor size distributions and fall velocities that complement traditional rain gauges and radar systems (Löffler et al., 1999).

The PARSIVEL2 (Particle Size Velocity, 2nd generation) disdrometer, manufactured by OTT HydroMet, is widely deployed in operational networks because it requires minimal maintenance and can classify precipitation types in real time (Tokay et al., 2014). The instrument records particle shadows crossing its laser beam to measure equivalent diameter and fall velocity; it then computes precipitation intensity ($\mathrm{mm\,h^{-1}}$) and classifies hydrometeor types. Despite these capabilities, many field studies have reported systematic biases in PARSIVEL2 measurements, particularly for solid precipitation (e.g., Zhang et al., 2015; Smith et al., 2020; Battaglia et al., 2010). For liquid precipitation, the instrument tends to register lower amounts than rain gauges (e.g., Annella et al., 2022; Ro et al., 2023), whereas for mixed precipitation, earlier versions reported higher values than weighing gauges (e.g., Licznar and Krajewski, 2016). To address these limitations, previous work has analyzed the recorded drop size distribution (DSD), compared mean values to empirical relationships, classified hydrometeors using density–diameter relations, or validated measurements using other instruments such as 2DVD cameras and snow gauges, including intercomparisons among disdrometers (e.g., Gualco et al., 2021). These efforts aim to establish relationships among diameter, velocity, density, and mass to characterize precipitation types at specific sites (Ishizaka et al., 2013).

This study evaluates and adjusts precipitation estimates from a PARSIVEL2 optical disdrometer using concurrent measurements from a weighing precipitation gauge at a high-altitude tropical glacier site in the Peruvian Andes. By comparing and combining these instruments, we assess the capabilities and limitations of the PARSIVEL2 for quantifying liquid and solid precipitation. We develop a method to improve PARSIVEL2 estimates by optimizing particle density assumptions and applying empirical diameter–velocity relationships for different hydrometeor types. Robust techniques for measuring precipitation in remote, high-altitude environments can support weather forecasting and water resource management in data-scarce regions.

2 Site and data

2.1 Area of study

The Huaytapallana glacier, protected by designation as a Regional Conservation Area, is 37 km from Huancayo and is the origin of Shullcas Basin, a main watershed in the central Andes of Peru. It encompasses a surface area of 22,406.52 ha (Fig. 1). This area ensures the protection and conservation of biological and landscape diversity, as well as water resources, which supply downstream cities. In an effort to analyze the impacts of climate change on precipitation in the Andean snow-capped mountains, measurement instruments were installed near the glacier zone at CEMGEM (Glaciers and Mountain Ecosystem Monitoring Center).The monitoring station is located at an altitude of 4709 m a.s.l., 11°56'18.06" S, and 75°4'9.44" W, approximately 2.5 km from the Huaytapallana Glacier System (see Fig. 1b).

The location of CEMGEM includes an area characterized by the periglacial conditions of the high mountain ecosystem adjacent to a tropical glacier. As a transition zone from the most intense cold to a cold surface due to seasonal action, recurring frost and snow are present (Pollard, 2018). The National Service of Meteorology and Hydrology of Peru (SENAMHI) classifies this area as very rainy with abundant humidity throughout the year and a semi-frigid climate. It has maximum temperatures of 13-15°C, minimum temperatures of 1 to 5°C, and annual precipitation ranging from 700-1200 mm.

Due to incomplete data records, a conditional daily mean precipitation was estimated for each month, calculated as the monthly total divided by the equivalent measured days (total records / 1440), as shown in Fig. 2c. Only three months were classified as reliable, with an observed data coverage equal to or greater than 80%: December, February, and March, which show mean daily precipitation values ranging from 4 to 5 mm/day. The remaining months present lower coverage; nonetheless, April, May, June, August, and September show estimated values between 2 and 4 mm/day. Given the irregular temporal distribution of rainfall records and the episodic nature suggested by the data, precipitation is analyzed through discrete events rather than by temporal climatological criteria. Precipitation in the area is driven by the adiabatic influence of humid air masses from the central jungle. The local orography facilitates the entry of humid fronts from the northeast (Espinoza et al., 2020); however, the dominant measured influence originates from the southeast Fig. 2d. During the transition and dry seasons, the primary moisture flux shifts toward the north, where the glacier is located Fig. 2d.

The average monthly temperature ranges from 2 to 4°C, increasing by one degree during the dry season months. There is an average standard deviation of 2.28°C for each month (Fig. 2a). The minimum temperature is 0°C and the maximum recorded temperature is 15°C in December, July, and August. Temperature and humidity show an inverse relationship throughout the study period. The average relative humidity ranges from 60 to 100%, with maximum values of 97 to 100% each month. In the tropical central Andes, there is an effect of ENSO; during El Niño events, higher temperatures are associated with a reduced and delayed accumulation of snow, opposite to La Niña events with cooler temperatures and greater accumulation of snow (Maussion et al., 2015).

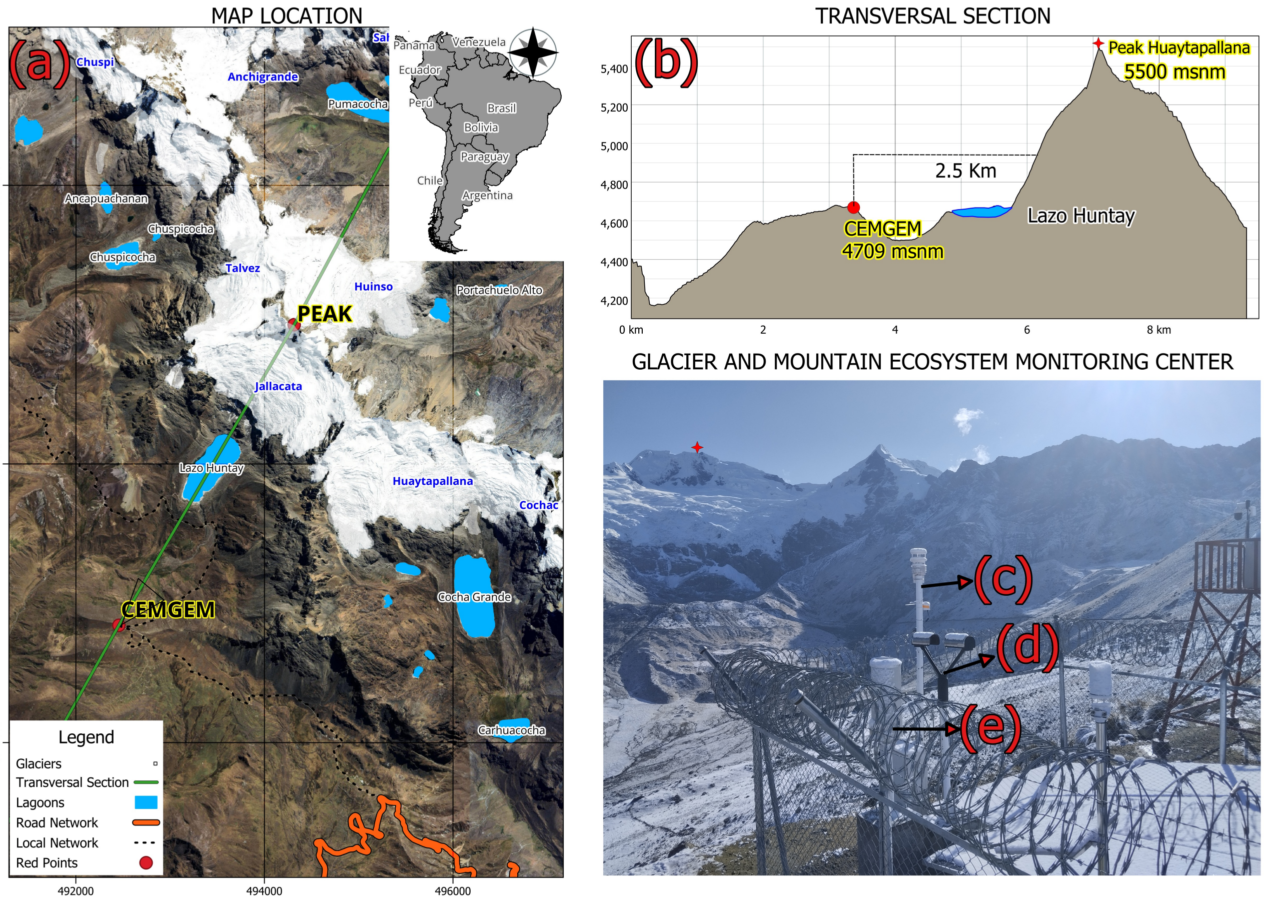

Figure 1. Area of study, (a) map of Huaytapallana glacier system and the environment. Basemap: satellite imagery © 2026 Airbus, © 2026 CNES / Airbus, accessed via © Google Earth Pro (image date: 12 April 2025); glacier coverage from Instituto Nacional de Investigación en Glaciares y Ecosistemas de Montaña (Base de datos INAIGEM, 2023. Cobertura del Inventario Nacional de Glaciares, Huaraz, Perú); digital elevation model: NASA/METI/AIST/Japan Space Systems, and U.S./Japan ASTER Science Team. ASTER Global Digital Elevation Model V003, 2019, distributed by NASA EOSDIS Land Processes DAAC, https://doi.org/10.5067/ASTER/ASTGTM.003; road network from Ministerio de Transportes y Comunicaciones (MTC), Plataforma Nacional de Datos Abiertos del Perú (Open Data Commons Attribution License), https://datosabiertos.gob.pe/. Red point marked CEMGEM location and Peak of the glacier. (b) Transversal cut shows the 2.5 km distance from the center to the accumulation zone of the glacier, and an overview of the instruments through the glacier: (c) Compact Station GMX500, (d) Optical Disdrometer PARSIVEL2, (e) Weighing Rain Gauge Pluvio2. The photo of instruments is courtesy of the TAMYA Project.

https://doi.org/10.5194/egusphere-2026-2705
Preprint. Discussion started: 8 July 2026

For wind speed, the variation is minimal, with monthly mean values ranging from 2.26 to 3.16 m s^{-1}. A maximum value of 15 m s^{-1} has been recorded in November, December, March, June, July, and August. Furthermore, a minimum of 0.30 m s^{-1} was recorded due to the 1-minute temporal resolution of the data (Fig. 2b). High wind speed affects snow cover, but also depends on the types of falling crystals (Mott et al., 2018). In glaciated catchments, wind speeds of 3 to 5 m s^{-1} are typically found. Due to the topography of the area, wind speed increases because of the acceleration or deceleration of air masses (Dadic et al., 2013).

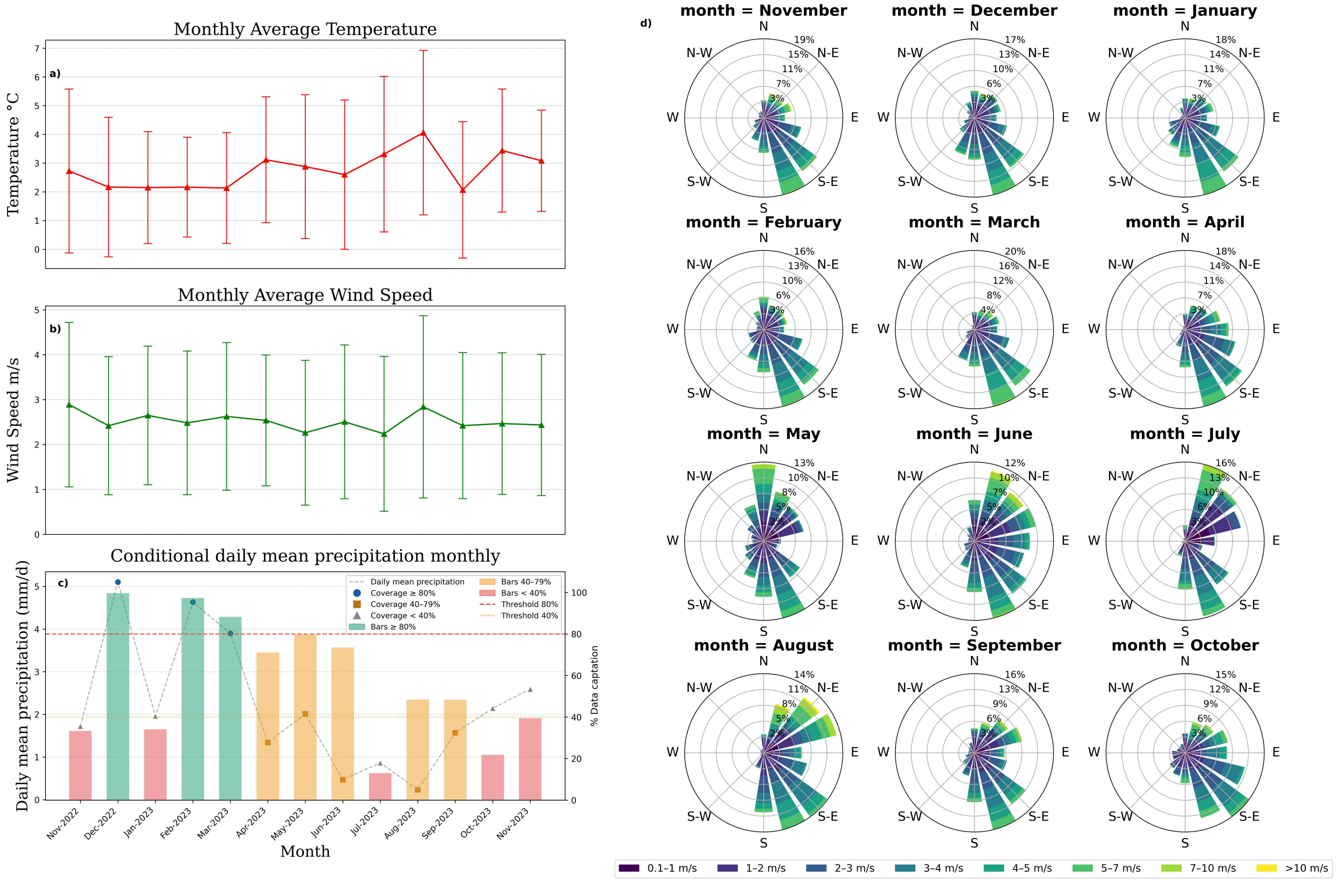

Figure 2. Atmospheric variables during the study period. (a) Average monthly temperature. (b) Average monthly wind speed. (c) Conditional daily mean precipitation. (d) Monthly wind direction.

2.2 Instruments and data

2.2.1 Weighing Precipitation Gauge

The Pluvio2 S weighing precipitation gauge manufactured by OTT HydroMet (Pluvio2, hereinafter) is a compact precipitation meter adapted for any climate. It meets the requirements established by the World Meteorological Organization (WMO) and

https://doi.org/10.5194/egusphere-2026-2705
Preprint. Discussion started: 8 July 2026

does not require constant maintenance. The compact design captures up to 400 mm (approximately 8 L) of precipitation in a 200 cm^2 collection (HydroMet, 2019). The instrument was installed 1.5 m above the surface, scheduled to record measurements every minute; see Fig. 1d. The generated variables are intensity and accumulated precipitation, with a range of 0-50 mm min^{-1} as a threshold for data validation.

The Pluvio2 is a highly reliable, accessible, and robust device for field measurement. The weighing method assists in measuring solid precipitation. It has demonstrated high reliability and resistance to extreme events (Grazioli et al., 2017; Tumbusch, 2003). At 6 s intervals, the instrument calculates the weight of the collecting container, including contents, with 0.001 mm resolution. It determines the intensity of precipitation by measuring the difference between the current and previous container weights. These values are then added to the total accumulated precipitation.

The instrument has demonstrated better performance than more traditional Tipping Bucket Rain Gauges (Colli et al., 2013), but is severely affected by strong wind speeds (Wauben and Pluvio, 2004). This factor can cause the registration of false particles and reduce efficient capture depending on particle size and type. The wind drags surrounding particles, generating non-representative area measurements. Double or single fences are usually installed to mitigate wind impact as recommended in the WMO report by BE Goodison et al. (1998). In addition, some research has generated functions to correct inefficient precipitation capture by the rain gauge, for example, (Kochendorfer et al., 2018) and (Jia et al., 2023). In the present study, a transfer function was applied, to correct the undercatch efficiency of a rain gauge without fence.

2.2.2 Compact Weather Station

The compact weather station GMX500 manufactured by Campbell Scientific was installed adjacent to Pluvio2. It records atmospheric variables such as temperature, humidity, ambient pressure, wind speed, and wind direction. The accuracy of the instrument at high altitude was evaluated by Valdivia et al. (2020).

2.2.3 Optical Disdrometer

The PARSIVEL2 is an optical disdrometer that simultaneously measures the size and falling speed of rain particles. It projects a horizontal laser beam (signal) at 780 nm in an area 30 mm wide, 180 mm long and 1 mm high. It consists of two housings protected by grilles: a laser emitter and a receiver. When a particle passes through the beam, it reduces the signal and voltage reaching the receiver. The amplitude of the deflected signal measures the size of particles, while the duration of the signal allows the calculation of fall velocity. This functionality is based on the physical principle of particle extinction (Löffler et al., 1999).

The instrument records direct measurements in its raw data variable, representing the relationship between 32 diameter classes with respect to 32 speed classes, grouped in a 32×32 matrix with 1024 total classes. The values are integers, displaying precipitation counts for a specific bin or coordinate (time, velocity). To reduce noise, the first two diameter classes (0.062, 0.187 mm) and the last two classes (21.5, 24.5 mm) do not record measurements. The instrument details variable formats and units in its user manual (HydroMet, 2019).

https://doi.org/10.5194/egusphere-2026-2705
Preprint. Discussion started: 8 July 2026

Table 1. Precipitation data filtering results showing the total amount of files (one each minute) and the total precipitation minutes duration for different filter applications

Date	Original	Filter1	Filter2	Filter3	Duration (min)
30/11/2022	4728	4727	4727	4727	540
31/12/2022	25639	25638	25638	25638	5225
31/01/2023	12703	12703	12703	12703	1391
28/02/2023	19880	19880	19880	19880	5671
31/03/2023	19442	19442	19442	19442	3486
30/04/2023	25244	25244	25244	25244	1026
31/05/2023	19148	19146	19146	19146	370
30/06/2023	4130	4129	4129	4129	179
31/07/2023	1423	1422	1422	1422	2
31/08/2023	7867	7867	7867	7867	7
30/09/2023	9427	9427	9427	9427	543
31/10/2023	1072	1072	1072	1072	115
30/11/2023	6035	6035	6035	6035	679

Original raw data files; Filter 1 (empty files), Filter 2(invalid characters) and Filter 3 (clean screen): processed data after sequential filtering steps

2.2.4 Quality Control

As a quality indicator, the sensor status variable records equipment issues: 0 indicates fair operation, 1-2 lens contamination, and 3 laser disorientations. This control was applied to the utilized data. PARSIVEL2 recorded all variables every minute, generating 1440 daily files of 6 KB each. Files containing invalid characters (non-standard UTF-8 encoding) were excluded from the analysis (see Table 1).

In the case of the Pluvio2, the catch efficiency (CE) equation and coefficients for an unshielded rain gauge proposed by (Kochendorfer et al., 2017) were applied, adjusting the precipitation amount measured by the Pluvio2.

3 Methods

3.1 Type Precipitation Identification

The PARSIVEL2 classifies precipitation using standardized meteorological codes, including SYNOP Tables 4680 and 4677, NWS codes, and METAR/SPECI Table 4678. SYNOP codes are part of the international meteorological observation system coordinated by the World Meteorological Organization (WMO), whereas METAR and SPECI codes come from standardized aeronautical meteorological reports (Shimazaki, 2019). These codes were designed to describe atmospheric conditions during

https://doi.org/10.5194/egusphere-2026-2705
Preprint. Discussion started: 8 July 2026

precipitation events. In operational practice, the precipitation phase (solid, liquid, or mixed) is strongly related to near-surface temperature and humidity; however, precipitation phase behavior and validation in tropical regions remain insufficiently studied (Fuchs' et al., 2001). The PARSIVEL2 uses these codes as a reference to classify precipitation types by mapping measured intensities (mm h^{-1}) to predefined intensity ranges. The identification is based on the number of hydrometeors recorded over fixed time intervals. The instrument assigns particles to 32 diameter–velocity classes, spanning diameters from 0.062 to 24.500 mm and fall velocities from 0.050 to 20.800 m s^{-1}.

3.2 Spectrum of precipitation

Precipitation types exhibit distinct microphysical characteristics such as size, shape, fall velocity, kinetic energy, and particle size distribution (PSD). These properties are useful for advancing cloud microphysics and for applications such as numerical weather prediction, remote-sensing retrievals, assessment of telecommunications attenuation, and studies of precipitation at the microscale. Particle size and fall velocity are among the most widely used variables to distinguish precipitation types. The PARSIVEL2 provides the PSD through $N(D)$, which represents the number of hydrometeors per unit air volume and per unit diameter interval, aggregated into diameter–velocity bins (i,j). We compute $N(D)$ using Eq. 1:

$$N(D) = \frac{1}{\mathrm{Time}} \sum_{i=1}^{n} \sum_{j=1}^{n} \frac{C_{ij}}{v_j \, \mathrm{Area}(D_i) \, \Delta D_i}, \tag{1}$$

where $N(D)$ is expressed in units of $\log_{10}(1\,\mathrm{m}^{-3}\,\mathrm{mm}^{-1})$. Here, ΔD_i is the width of the i-th diameter bin (mm), and D_i is the representative diameter of that bin (mm). The instrument uses $n = m = 32$ diameter and velocity bins. The effective sampling area, $\mathrm{Area}(D_i)$, accounts for the finite beam geometry and is computed from a light sheet of dimensions $180\,\mathrm{mm} \times (30\,\mathrm{mm} - D_i/2)$ (mm^2). The sampling interval is $\mathrm{Time} = 60\,\mathrm{s}$. The fall velocity of the j-th velocity bin is v_j ($\mathrm{m\,s}^{-1}$). Finally, C_{ij} is the number of particles counted in bin (i,j), obtained from the raw disdrometer output (`raw_data`).

From the PSD, the instrument derives additional variables, including particle count, reflectivity, snow intensity, kinetic energy, and precipitation intensity. Precipitation intensity is expressed in mm h^{-1} and is computed using Eq. 2, where $V(D)$ is the mean fall velocity for each diameter (m s^{-1}) and ρ is the particle density (g cm^{-3}).

$$R = \frac{6\pi}{10^4} \int_{D_{\min}}^{D_{\max}} \rho \, N(D) \, V(D) \, D^3 \, dD, \tag{2}$$

Precipitation intensity at the ground depends on both fall velocity and hydrometeor water content. Because terminal fall velocity depends in part on particle density, higher densities generally imply higher fall speeds. Here, ρ denotes the density of liquid water ($\sim 1\,\mathrm{g\,cm}^{-3}$) or other hydrometeor types. Accurate conversion of measured size distributions and fall velocities into precipitation intensity therefore requires appropriate density assumptions.

3.3 Precipitation estimates correction

The correction method consists of three components. First, precipitation events are identified, and the analysis is performed on an event basis. Second, segmentation masks are applied for each hydrometeor category. Third, precipitation intensity (Eq. 2) is recomputed using bulk density values for each category. Finally, corrected precipitation totals are calculated for each event. 170 Figure 3 summarizes the workflow.

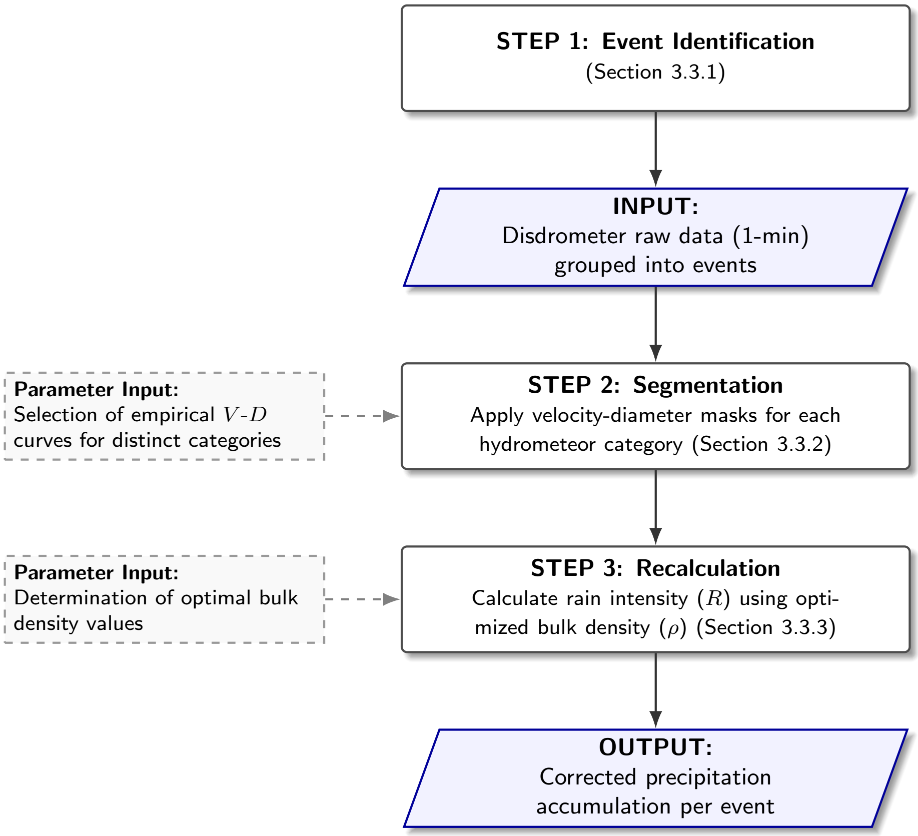

Figure 3. Flowchart of the precipitation correction process showing the three main stages: event determination, data segmentation by category, and rain intensity calculation.

3.3.1 Definition of precipitation events

Criteria to define a precipitation event

Because the disdrometer is highly sensitive, it can detect isolated particles during non-precipitating periods, and short low-intensity intervals can introduce noise. We therefore applied the criteria of Tokay et al. (2014) to define precipitation events, 175 using thresholds for intensity (>0.1 mm h^{-1}), total particle count (>10), and dry gaps shorter than 120 min. This approach has been widely used and effectively reduces noise, particularly for light precipitation (e.g., Ma et al., 2019; Zeng et al., 2021; Valdivia et al., 2024).

Criteria to select precipitation events

The analysis focuses on the events detected by both instruments and on reducing noise from light precipitation. Therefore, a threshold was established considering the limitations of both instruments:

- Events with zero accumulated precipitation were excluded.
- The sensitivity of the disdrometer was used to select events lasting longer than 10 minutes, thus avoiding the recording of very light and intermittent precipitation.
- Because the reference rain gauge lacked wind shielding, we first applied a transfer function to correct undercatch due to wind. We then retained events with accumulated precipitation >0.25 mm to reduce noise from very light precipitation in the gauge record, following Kochendorfer et al. (2017).

3.3.2 Hydrometeor types segmentation

The relationship between hydrometeor diameter and fall velocity follows from the balance between gravitational and drag forces as particles fall through air. This balance was first modeled by Gunn and Kinzer (1949), leading to the widely used power-law form $v = aD^b$, where v is terminal velocity, D is diameter, and a and b are empirically derived constants. According to the manufacturer, liquid precipitation types are segmented using this empirical curve. Footec and Toit (1969) proposed a correction for non-sea-level conditions by accounting for air-density variations with altitude, which has been validated at multiple altitudes (i.e., Bringi et al., 2018; Valdivia et al., 2020). For reclassification, we selected five hydrometeor categories based on empirical curves reported in the literature (Table 2).

All these empirical equations were selected considering the resulting curves align with the diameter and fall velocity values of particles recorded by the field disdrometer. Using these curves, the five categories serve as a segmentation mask as shown in Fig. 3.

Classification boundaries were defined as follows:

- **Rain and Drizzle:** Particles were reclassified as rain if their velocity–diameter values fell within ±50% of the Gunn and Kinzer (1949) curve, adjusted for a correction factor due the altitude (4709 m a.s.l.) following Footec and Toit (1969) in Fig. 11a.
- **Snow:** We applied all empirical curves representing aggregated snow crystals and some other types in Fig. 11d. These curves define the expected velocity range for snow particles from 0.5 to tha last bin value diameter (24.5 mm).
- **Graupel:** Following Locatelli and Hobbs (1974), graupel particles were identified in the diameter range 0.5-5 mm with terminal velocities intermediate between snow and hail in Fig. 11c.

Table 2. Empirical fall velocity equations for different hydrometeor categories and types

Hydrometeor Categories	**Hydrometeor Types**	**Diameter Ranges (mm)**	**Empirical Fall Velocity Equation (m s^{-1})**	**References**
Rain	Raindrops	$d < 5$	$v = (9.65 - 10.3e^{-0.6d})C$	Gunn and Kinzer (1949); Footec and Toit (1969)
Wet Snow	Wet Snow	$0.6 \leq d \leq 9$	$v = 4.65 - 5e^{-0.95d}$	Fehlmann et al. (2020)
Snow	Unrimed side planes	$0.4 \leq d \leq 1.2$	$v = 0.81d^{0.99}$	Locatelli and Hobbs (1974)
	Densely rimed dendrites	$0.8 \leq d \leq 4$	$v = 0.62d^{0.33}$	Locatelli and Hobbs (1974)
	Aggregate of unrimed radiating assemblages	–	$v = 0.69d^{0.41}$	Locatelli and Hobbs (1974)
	Aggregate of unrimed side planes	–	$v = 0.82d^{0.12}$	Locatelli and Hobbs (1974)
	Aggregate of unrimed radiating assemblages	$2 \leq d \leq 12$	$v = 0.79d^{0.27}$	Locatelli and Hobbs (1974)
	Aggregate of densely rimed radiating assemblages	$2 \leq d \leq 10$	$v = 0.8d^{0.16}$	Locatelli and Hobbs (1974)
	Densely rimed aggregates	–	$v = 1.1d^{0.15}$	described in Ishizaka et al. (2013)
	Rimed aggregates	–	$v = 0.96d^{0.12}$	described in Ishizaka et al. (2013)
	Dendrite	–	$v = 0.3$	Nichols (1954)
Graupel	Lump Graupel	$0.5 \leq d \leq 5$	$v = 1.6d^{0.46}$	Locatelli and Hobbs (1974)
	Lump Graupel	–	$v = 1.5d^{0.37}$	Locatelli and Hobbs (1974)
	Lump Graupel	–	$v = 1.3d^{0.66}$	Locatelli and Hobbs (1974)
	Hexagonal Graupel	–	$v = 1.1d^{0.57}$	Locatelli and Hobbs (1974)
	Conical Graupel	–	$v = 1.2d^{0.65}$	Locatelli and Hobbs (1974)
	Graupel like snow of lump type	–	$v = 1.1d^{0.28}$	Locatelli and Hobbs (1974)
	Graupel like snow of hexagonal type	–	$v = 0.86d^{0.25}$	Locatelli and Hobbs (1974))
Hailstones	Fresh Hailstones	$5 \leq d \leq 25$	$v = 8.44(0.1d)^{0.553}$	C. and J. (1983)
	Soaked Hailstones	–	$v = 10.58(0.1d)^{0.267}$	C. and J. (1983)
Hail	Hail	$d \geq 10$	$v = 12.43(0.1d)^{0.5}$	Allen et al. (2020)
	H1	–	$v = 5.23(0.1d)^{0.65}$	Heymsfield and Wright (2014)
	H2	–	$v = 12.07(0.1d)^{0.64}$	Heymsfield and Wright (2014)
	H3	–	$v = 4.88(0.1d)^{0.84}$	Heymsfield and Wright (2014)

d represents particle diameter. Velocity equations are applicable within the specified diameter ranges where indicated.

https://doi.org/10.5194/egusphere-2026-2705
Preprint. Discussion started: 8 July 2026

- **Hail:** True hail was restricted to particles >10 mm diameter with velocities >8 m s^{-1}, consistent with densities approaching solid ice (0.9 g cm^{-3}; Heymsfield and Wright (2014). Given the study site characteristics and observed maximum velocities (<14 m s^{-1}), most large frozen particles were reclassified as soft hail rather than hard hail in Fig. 11b.

- **Exclusion of Spurious Detections:** Particles >10 mm with velocities <1 m s^{-1} were flagged as measurement artifacts (e.g., insects, debris, edge-of-beam particles) following Gualco et al. (2021) and excluded from analysis.

- **Wet Snow/Mixed Phase:** The transition region between rain and graupel velocity-diameter spaces likely contains wet snow and mixed-phase particles. While we acknowledge this complexity, detailed classification of transitional states is beyond the scope of this study. So, we extented the range from 0.6 to the last bin value diameter (24.5 mm).

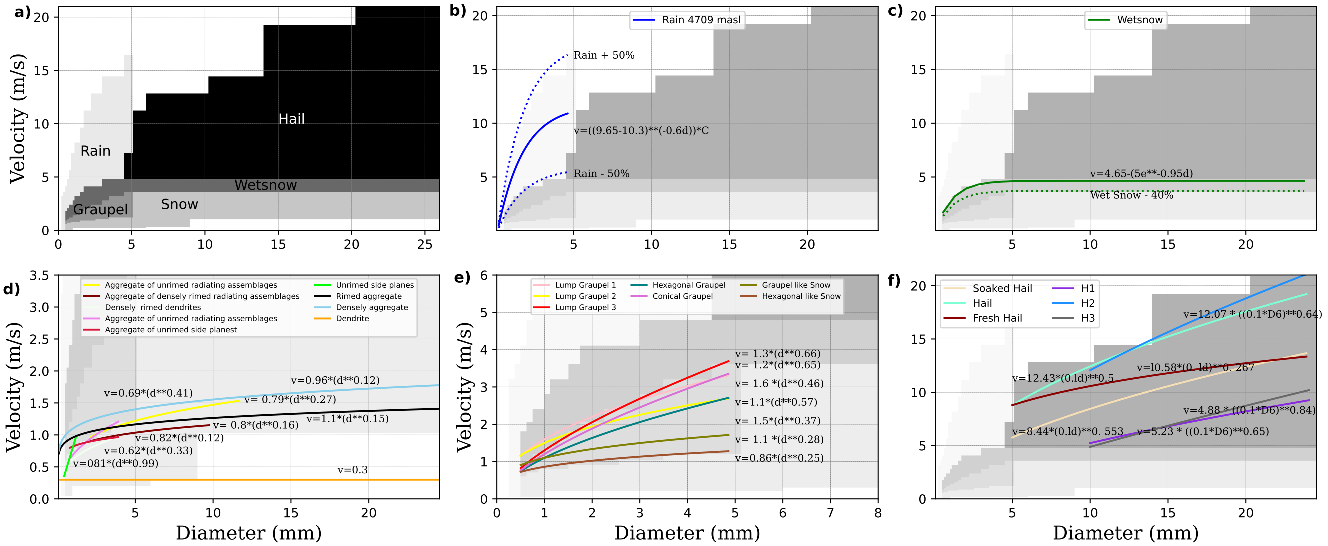

Figure 4. Empirical velocity–diameter (V-D) curves used for hydrometeor segmentation (Table 2). (a) The complete five-category segmentation mask (rain, drizzle, snow, wet snow, graupel, hail), showing how each category occupies a distinct region of the V-D space; this segmentation (gray shading) is repeated as background in panels (b)–(f) for reference. (b) The rain curve corrected for altitude (4709 m a.s.l.), with two auxiliary curves (±50%) marking the segmentation boundary used to reclassify particles as rain. (c) The wet snow curve. (d) All snow-type curves. (e) All graupel-type curves. (f) Curves for hailstone sub-types.

3.3.3 Recalculate the intensity rate

As shown in Equation 2, intensity rate calculation requires the density value. Considering the differences in bulk density for each hydrometeor type, we established a range of density values found in previous research (see reference column in Table. 2).

Density values are calculated through the mass-volume relationship of particles. Since direct measurements of particle dimensions and weight are challenging, various studies have established empirical equations relating mass to diameter and density to diameter, validated through field observations and particle capture. There is a relationship between hydrometeor

https://doi.org/10.5194/egusphere-2026-2705
Preprint. Discussion started: 8 July 2026

type and density that influences fall velocity, as density determines the drag force on particles as they fall. In this study, lacking direct particle observations, disdrometer estimations combined with empirical curves from literature were used to establish density ranges for 5 hydrometeor categories:

- Considering all graupel types proposed by Locatelli and Hobbs (1974), density values range from 0.05-0.45 g cm^{-3}. Additional research found ranges from 0.07 to 0.45 g cm^{-3} (diameter 0.5-1.0 mm) and 0.45 to 0.25 g cm^{-3} (diameter 1.0-2.0 mm) for lump graupel (Zikmunda and Vali, 1972). All types were grouped as Locatelli and Hobbs (1974) noted that various graupel values reflect natural diversity. Classification followed Magono and LEE (1966), based on solid particles sampled in Japan, not considering arctic or tropical glacier types.

- Snow density is influenced by multiple factors including crystal structure, size, fall velocity, temperature, and riming processes (Ishizaka et al., 2013). While existing research has predominantly focused on sub-zero temperatures, significant knowledge gaps remain regarding snow behavior at or near 0°C. At this critical temperature, the most common snow type is the 'aggregate' (Hobbs et al., 1974), characterized by diameters exceeding 15 mm or equivalent volume diameters of 31 mm under calm wind conditions at 0.7°C (Brandes et al., 2008). Simulation studies have revealed important relationships between snow density, size, and fall velocity. Maruyama (2005) demonstrated that snowflakes with a density of 0.1 g cm^{-3} and melted diameters ranging from approximately 0.5 mm to 3-4 mm exhibit fall velocities between 0.5 m s^{-1} and 1.5 m s^{-1}. For higher density snowflakes (0.3 g cm^{-3}), similar diameter ranges (0.5 mm to 3-4 mm) produce increased fall velocities ranging from approximately 1.0 m s^{-1} to 2.0 m s^{-1}. For dry and pure snow conditions, established research has considered density values ranging from 0.05 to 0.35 g cm^{-3} (Szyrmer and Zawadzki, 2010; Zawadzki et al., 2005). Based on these previous studies we will adopt the comprehensive density range of 0.05 to 0.35 g cm^{-3}.

- Wet snow represents a distinct mixed-phase hydrometeor consisting of partially melted snowflake aggregates where liquid meltwater adheres to the ice crystal structure, exhibiting unique fall characteristics that differ significantly from dry snow conditions. Observational studies by (Yuter et al., 2006) at temperatures between 0 and 0.5°C revealed a notably weak relationship between particle diameter and fall velocity, with exceptionally high variability characterized by standard deviations of 120% to 230% relative to dry snow measurements. These studies documented wet snow particles with diameters reaching up to 11 mm and estimated a characteristic density of 0.1 g cm^{-3} (10^5 g m^{-3}), while very large aggregates greater than 13 mm tend to disappear as they undergo complete melting into large raindrops. Independent research by Zawadzki et al. (2005) reported higher wet snow densities of approximately 0.2 g cm^{-3}. Based on these specific observational studies, a representative density range of 0.1 to 0.2 g cm^{-3} emerges as appropriate for wet snow hydrometeors.

- Hailstones exhibit intermediate characteristics between graupel and true hail, with density values that vary significantly based on particle size. For smaller hailstones, C. and J. (1983) reported density ranges of 0.31-0.61 g cm^{-3}, while larger hailstones with diameters exceeding 10 mm and extending up to 60 mm typically exhibit higher densities ranging from

https://doi.org/10.5194/egusphere-2026-2705
Preprint. Discussion started: 8 July 2026

0.84 to 0.9 g cm^{-3} (Allen et al., 2020). This density increase with size reflects the enhanced compaction and ice structure development that occurs during the growth process of larger hailstones.

- Raindrops reach terminal velocity through the balance between gravitational force and air resistance. While water density is constant at 1 g cm^{-3}, the effective density of raindrops can be lower due to shape deformation, particularly for larger drops that become flattened and oval shaped during fall. However, this concept is debated for the smallest drops (<0.47 mm diameter, classified as drizzle) where shape effects are minimal. For this study, a density range of 0.9 to 1.0 g cm^{-3} is adopted based on disdrometer measurements representing 50% of observed liquid precipitation types.

The density values were determined by correlating the total precipitation adjusted measurements adjusted from the weighing rain gauge to the theoretical density combinations for each types of hydrometeor. The optimal bulk density for each type was selected based on the best fit and lowest RMSE values. Once density values were determined, precipitation was recalculated by changing the density values and intensity rate for each type according to the segmentation as follows:

$$P_{\text{corrected}} = P_{\text{rain}} \cdot \rho_{\text{rain}} + P_{\text{snow}} \cdot \rho_{\text{snow}} + P_{\text{wet snow}} \cdot \rho_{\text{wet snow}} + P_{\text{graupel}} \cdot \rho_{\text{graupel}} + P_{\text{soft hail}} \cdot \rho_{\text{soft hail}} \tag{3}$$

Finally, the mean absolute error (MAE), the coefficient of linear regression determination (R^2), and the root mean square error (RMSE) were used to compare the corrected precipitation events between the disdrometer and the weighing rain gauge.

4 Results

4.1 Precipitation characterization according to PARSIVEL2

According to the PARSIVEL2 classification based on SYNOP Table 4680, the most frequent precipitation type during the study period was drizzle with rain, representing 30.42% of all recorded minutes, whereas hail was the least frequent (30 min; Fig. 5).

Excluding the mixed phase, liquid precipitation (rain, drizzle with rain, and drizzle) accounted for about half of the observations, compared with 46.63% for the solid phase. Near-surface meteorological conditions influence the persistence of each hydrometeor type. Based on measurements from the compact weather station, we summarize typical conditions below.

For drizzle, the median wind speed, temperature, air pressure, and relative humidity were 2.4 m s^{-1}, 2.9°C, 582.3 hPa, and 96.5%, respectively (see Fig. 6). This precipitation type is typically associated with stratus and stratocumulus clouds (Cadeddu et al., 2020). In weak updraft low layer clouds, these smaller droplets form by coalescence, with high relative humidity below clouds preventing evaporation before falling to the ground. Similar atmospheric conditions are found in drizzle with rain.

Hailstones form in strong convective updrafts that repeatedly loft liquid drops above the freezing level, where they freeze and accrete additional water and ice (Allen et al., 2020). They may initiate as graupel or ice pellets and grow through successive riming cycles. Air pockets trapped during growth reduce the bulk density, which can lead to soft hail at the surface. Median near-surface conditions during soft-hail minutes were 0.7°C, 98.1%, 2.9 m s^{-1}, and 582.5 hPa for temperature, relative humidity,

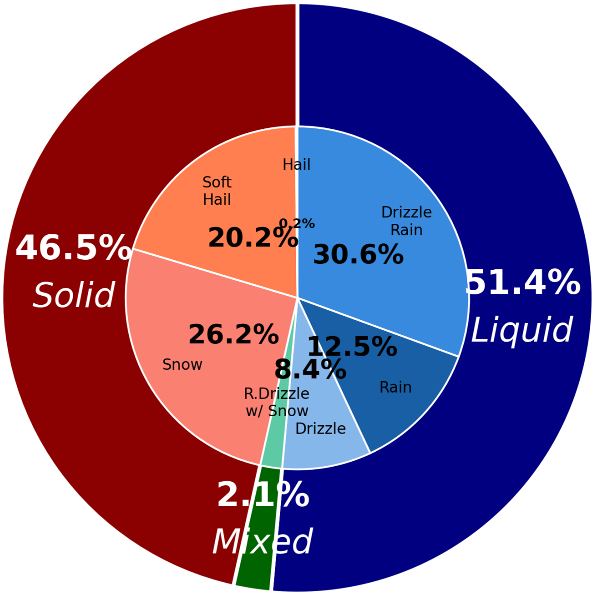

Figure 5. Classification of hydrometeor types according to SYNOP Table 4680 from the disdrometer minute data. The inner pie chart shows each precipitation type, while the outer ring groups the observations into liquid, solid, and mixed phases.

wind speed, and air pressure, respectively. In the Mantaro Valley of Peru, the term “granizo” (hail) is widely used to describe a broad range of falling ice particles (Valdivia et al., 2024). Although hail represented only 0.16% of total precipitation in the study area, these events are among the most impactful in the valley. The median temperature during hail was similar to that during snow (-0.1°C), and the median wind speed ($3\,\mathrm{m\,s^{-1}}$) was comparable to most other hydrometeor types except snow.

For snow, minutes with high wind speeds (up to $11\,\mathrm{m\,s^{-1}}$) were recorded, with surface temperatures up to 4°C. However, the interquartile ranges were 1–$2.8\,\mathrm{m\,s^{-1}}$ for wind speed and -0.3 to 0.2°C for temperature, which is consistent with typical near-surface conditions for snowfall. Note that these meteorological variables are measured at the surface; snow can remain solid while falling even when near-surface temperatures are a few degrees above 0°C, depending on humidity and melting time scales (National Snow and Ice Data Center, n.d.). Snow consists of ice crystals whose habit and degree of aggregation are strongly influenced by the thermodynamic and dynamical environment; under strong winds, crystals can fragment and become more compact.

Among precipitation types, temperature shows the clearest separation among phases. As observed in Fig. 6, liquid types exhibit the highest temperatures, solid types the lowest temperatures, and the mixed phase (rain drizzle with snow) falls in between. All categories also include occasional atypical wind-speed values, which likely reflects the 1-min temporal resolution: rapid transitions within a minute can be mapped to a single class. Atmospheric variables are not measured by the PARSIVEL2; therefore, its minute-by-minute classification is driven primarily by particle diameter and fall velocity and cannot explicitly account for evolving surface conditions during phase transitions.

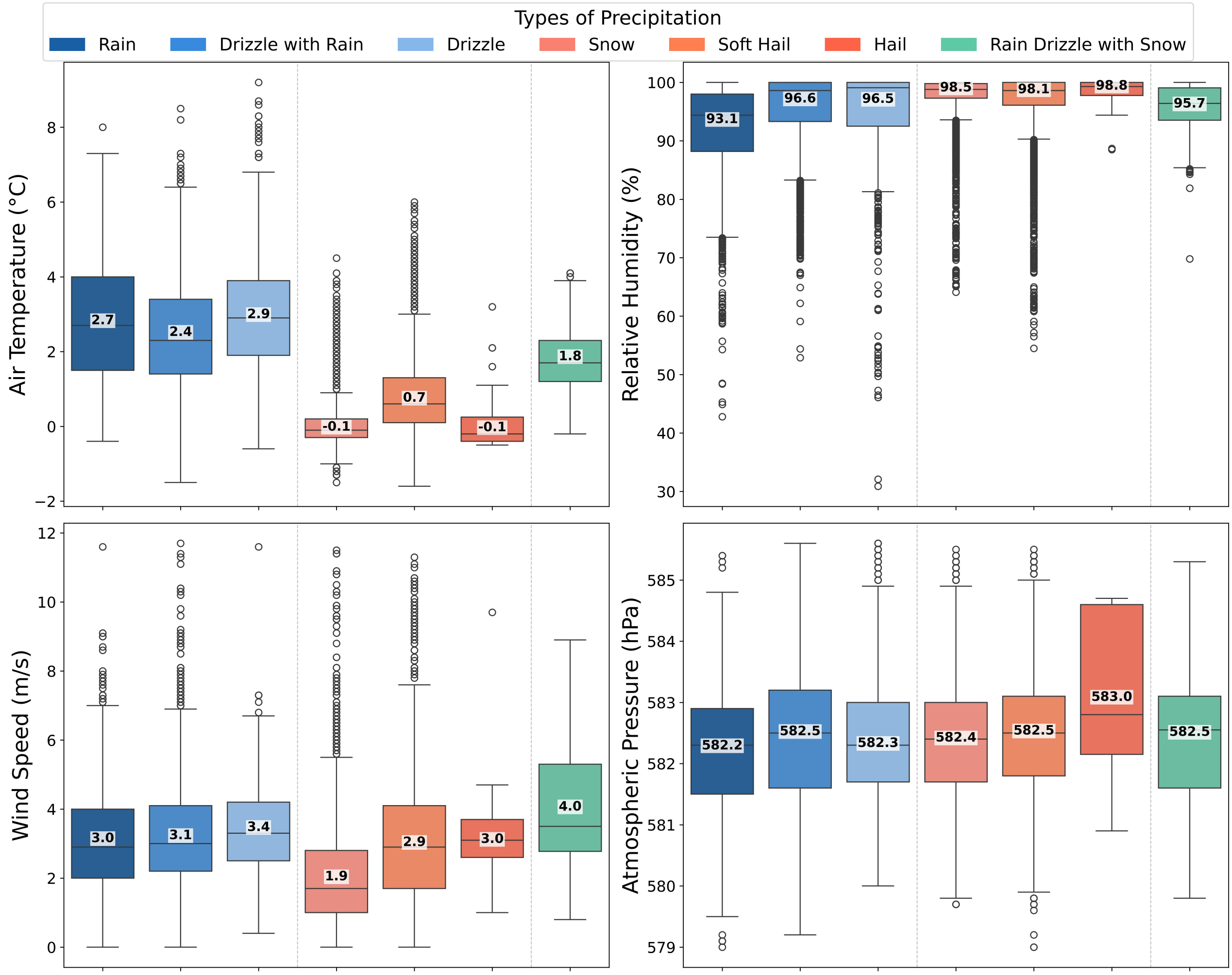

Figure 6. Distribution of temperature, wind speed, relative humidity and atmospheric pressure values considering the different hydrometeor types identified by the disdrometer PARSIVEL2 minute data. The boxplots for each atmospheric variable show the distribution of all recorded data, with the mean value labeled inside each box. The gray line separates the liquid, solid, and mixed phase groups.

4.2 Performance evaluation and error quantification

4.2.1 Assessment of the PARSIVEL2

For all precipitation types, the PSD peaked at small diameters and decreased with increasing diameter, with each precipitation type exhibiting a characteristic maximum diameter. Snow particles were detected across diameters ranging from 0.34 to 19 mm. Since the instrument measures equivalent spherical diameter and fall velocity without imaging capabilities, the recorded particles may represent individual snow crystals, aggregated snowflakes, or rimed particles.

Individual snow crystals typically measure 0.5-5 mm (Straka, 2009), while aggregated snowflakes under favorable conditions (temperatures near 0°C, high humidity) can exceed 25 mm in diameter (Lawson et al., 1998; Locatelli and Hobbs, 1974). The maximum observed diameter of 19 mm is consistent with aggregated snowflakes commonly reported in winter precipitation events.

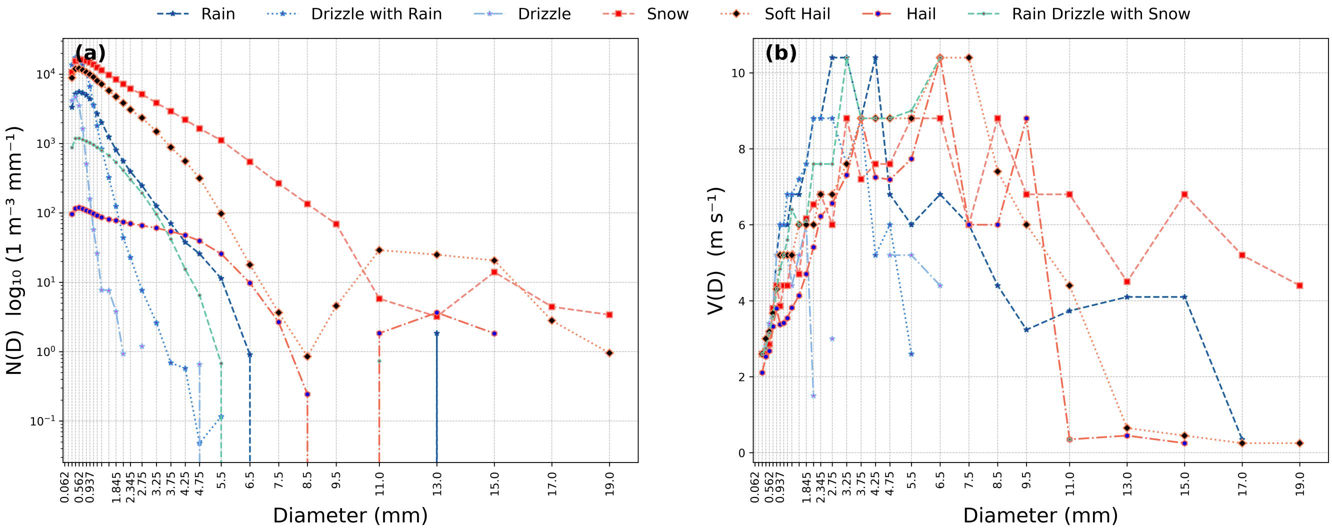

Figure 7. Drop size distribution (a) and maximum mean fall velocity per diameter bin (b), both decreasing with increasing particle diameter. Data are grouped by precipitation type, each identified by a distinct combination of line style and marker shape: rain (dashed line, star marker, dark blue), drizzle with rain (dotted line, star marker, medium blue), and drizzle (dash-dot line, star marker, light blue) share the star marker but are distinguished by line style and color shade, reflecting their common liquid-phase origin. The remaining types use unique marker shapes: snow (dashed line, square marker, red), soft hail (dotted line, diamond marker, orange), hail (dash-dot line, hexagon marker, tomato), and rain drizzle with snow (dashed line, dot marker, green).

Rain particles were classified by the instrument across diameters from 0.34 to 13 mm, with the bulk of detections below 4 mm (see Fig. 7a). This range extends beyond the natural raindrop maximum of approximately 8.8 mm documented under extreme conditions (Hobbs and Rangno, 2004), indicating potential misclassification. Drizzle particles were predominantly classified below 1.87 mm, which is inconsistent with meteorological definitions that typically limit drizzle to < 0.5 mm; moreover, di-

https://doi.org/10.5194/egusphere-2026-2705
Preprint. Discussion started: 8 July 2026

ameters extended up to 4.5 mm, substantially overlapping with the rain size distribution. This overlap suggests limitations in the instrument's automated discrimination algorithm, particularly during mixed precipitation conditions. Hail particles were detected up to 15 mm diameter, while soft hail reached 19 mm. However, both types showed substantial detections below 5 mm, which conflicts with field observations where hailstones typically range from 5 to 19 mm (Allen et al., 2020), suggesting misclassification of small frozen particles as hail.

To investigate classification accuracy, we analyzed the maximum mean fall velocity recorded within each diameter bin for all hydrometeor types (see Fig. 7b). The instrument calculates mean velocities for 32 diameter ranges; we extracted the highest mean velocity value within each bin to approximate the upper envelope of the velocity–diameter relationship for each category. Several physically inconsistent patterns emerged:

- Rain particles at diameters >6 mm exhibited maximum mean velocities of only 4 m s^{-1}, substantially below the expected terminal velocity of 8-9 m s^{-1} for raindrops of this size.
- Mixed precipitation, rain-drizzle, and snow types showed maximum mean velocities reaching 10 m s^{-1} at diameters <6.5 mm, exceeding theoretical terminal velocities for liquid drops and snow particles of these sizes.
- Conversely, hail and soft hail at diameters >10 mm recorded maximum mean velocities near 0 m s^{-1}, which is physically implausible for falling particles of this size and density.

These velocity-diameter inconsistencies indicate systematic misclassification by the instrument's automated algorithm. According to the manufacturer (Nemeth and Beck, 2011), the classification relies on the empirical velocity-diameter relationship of Gunn and Kinzer (1949) for rain. To assess the validity of this approach across all hydrometeor types, we compared the instrument's classified particle distributions against established empirical curves (see Table. 2, Fig. 8). The graphs show the relation of diameter and velocity falls of each precipitation types registering by the disdrometer. Each type is correlating with the empirical curves of each precipitation types.

This discrepancy arises because the instrument classifies particles on a minute by minute basis, during which multiple precipitation types often coexist simultaneously. The resulting misclassification propagates into derived variables such as drop size distribution, rainfall intensity, and reflectivity which are calculated using all detected particles within each minute regardless of type. Additionally, the instrument's assumptions about particle shape (spherical for D<1 mm; variable axial ratios of 1.0-0.7 for 1-5 mm) introduce further uncertainties, particularly for snowflakes where measured width can differ substantially from actual dimensions (Battaglia et al., 2010). These geometric errors are amplified at larger diameters due to the D^3 term in volume calculations. The combined effects of misclassification and shape assumptions result in systematic biases in precipitation accumulation estimates. To quantify these biases under operational conditions, we compare the PARSIVEL^2 measurements against weighing rain gauge over the study period.

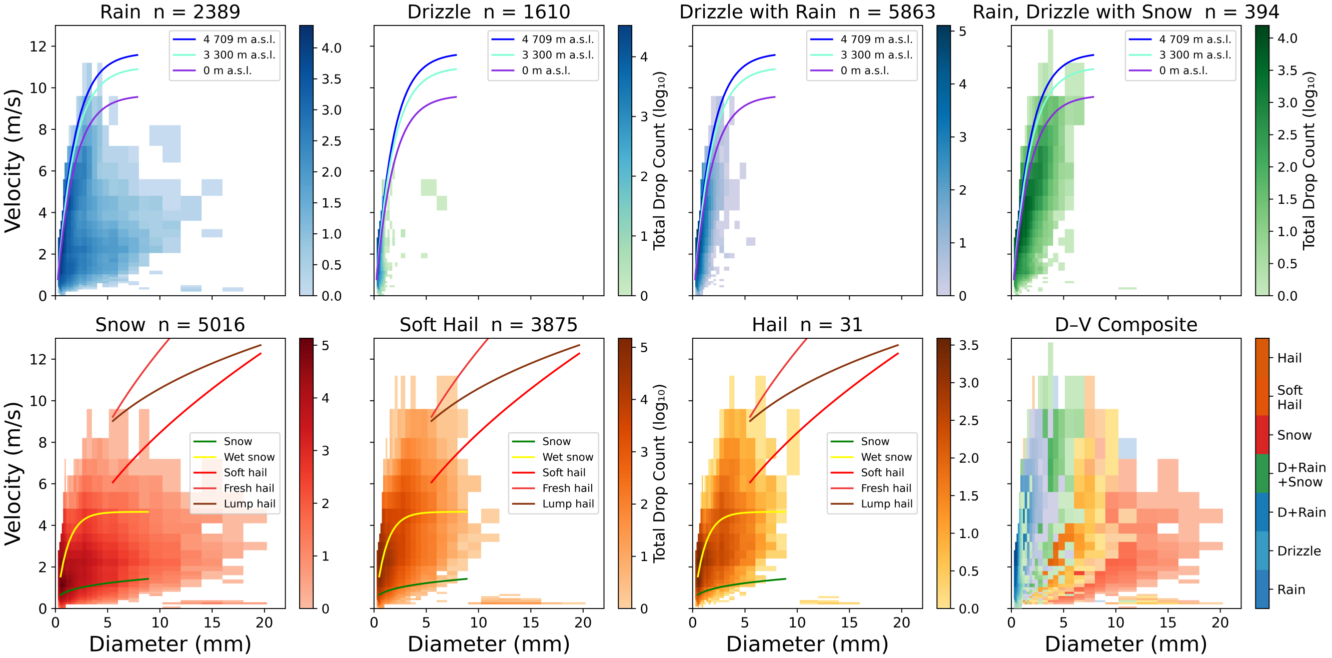

Figure 8. Raw diameter–velocity data grouped by classified precipitation type, compared against empirical fall-velocity curves. Each panel uses an independently scaled, type-specific colormap to show drop concentration ($\log_{10}$ scale). Top row: liquid and mixed types, with the Gunn and Kinzer (1949) terminal velocity curve corrected for altitude following Foote and Toit (1969), at 4709 m a.s.l. (blue), 3300 m a.s.l. (cyan), and sea level (purple). Bottom row: solid types, with five reference curves for snow, wet snow, soft hail, fresh hail, and lump hail. The D-V Composite panel (bottom right) overlays all seven types using a fixed discrete color per type for legibility, distinct from the continuous colormaps used elsewhere in the figure.

4.2.2 Impact on Precipitation Accumulation

To evaluate the impact of classification errors on precipitation accumulation, we compared PARSIVEL2 measurements against an independent OTT Pluvio2 weighing rain gauge. Both instruments record at 1-minute resolution. After applying the event definition criteria, we identified 129 events; however, this number was reduced to 70(54.3%) after applying the selection criteria. 3.3.1. Fifteen events (11.6%) recorded a duration of less than 10 minutes, 34 events (26.3%) were not detected by the Pluvio2, and 10 events (7.8%) recorded less than 0.25 mm as measured by the weighting rain gauge.

To systematically address the most problematic cases, we identified 14 "extreme events" defined as those exceeding the 95th percentile of precipitation amount distribution (>10.6 mm; equivalent to Q3 + 1.5 × IQR). These extreme events, marked with yellow labels, contribute disproportionately to the overall RMSE and will serve as benchmark cases for evaluating the correction methodology presented in Section 4.3 (Fig. 13). Events were categorized into three phases based on predominant precipitation type: "solid" (≥80% snow/graupel/hail), "liquid" (≥80% rain/drizzle), and "mixed" (remainder). This 80% thresh-

https://doi.org/10.5194/egusphere-2026-2705
Preprint. Discussion started: 8 July 2026

old ensures dominant phase representation while allowing minor contamination from transitional periods. As result we got,16 liquid events, 17 solid events, and 38 mixed events. Which were analysed by a lineal regresion.

- **Liquid precipitation (Fig.13a):** The instruments show excellent agreement ($R^2 = 88.69\%$) with a negligible mean bias ($+0.00$ mm) and low error metrics (RMSE = 0.71 mm; MAE = 0.40 mm). The positive intercept (0.176) indicates that the PARSIVEL^2 is highly sensitive to light precipitation. However, despite the zero overall bias, a relative overestimation of $+15.7\%$ is observed in low-intensity events (mostly < 2 mm). Conversely, for higher intensities, the instrument tends to underestimate precipitation compared to the PLUVIO^2, as reflected by a slope of 0.918.
- **Solid precipitation (Fig. 13b):** Exhibits a substantial overestimation, despite a high correlation coefficient ($R^2 = 85.15\%$). The PARSIVEL^2 shows a mean overestimation of $+84.1\%$, with a significant bias of $+7.09$ mm and an RMSE of 13.05 mm. The slope of 2.103 confirms that the instrument systematically records more than double the reference values. This discrepancy is further evidenced by specific extreme events (e.g.,2,14,22,26,80), where the disdrometer overestimated the PLUVIO^2 measurements by factors ranging from 1.3 to $4.2\times$."
- **Mixed precipitation (Fig. 13c):** Represents the most frequent category ($n = 37$), accounting for over half of the sampled events. While it exhibits the highest correlation ($R^2 = 95.02\%$), it also records the most severe systematic overestimation ($+98.5\%$) with a slope of 1.936. At an altitude of 4709 m a.s.l., the frequent coexistence of different hydrometeor phases leads to significant errors in the PARSIVEL^2 default rain rate (R) calculation, which assumes the density of liquid water for large particles. The extreme discrepancies observed in events (3,15,16,52,62,64,83,102,118) highlight the instrument's inability to reconcile the optical diameter of melting hydrometeors with their actual mass, leading to a substantial inflation of the intensity values compared to the PLUVIO^2 reference.

The discrepancy regarding events not registered by the Pluvio2 reflects differences in instrument sensitivity rather than measurement failure: the PARSIVEL2 optical detection principle enables it to identify light precipitation events (<1.8 mm accumulated; Fig. 9), that fall below the Pluvio2 minimum detection threshold of 0.1 mm/min (intensity resolution) during all events. These undetected events were predominantly characterized by drizzle, light rain, and brief snow flurries. Conversely, the events showing the greatest overestimation by the PARSIVEL2 (see yellow label in Fig. 9) were dominated by snow, soft hail, and hail, with typical durations exceeding 1 hour. The extended duration of these events increases the cumulative impact of the classification errors documented in the previous section, where the presence of multiple hydrometeor types within individual minutes contaminates the precipitation calculations.

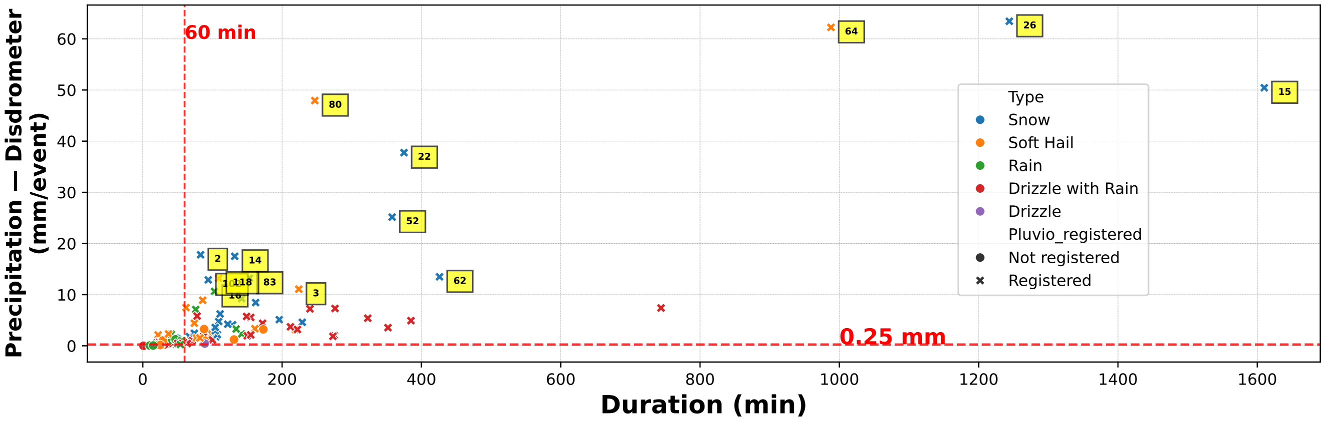

Figure 9. Comparison the amount of precipitation determined by Parsivel2 and Pluvio2 with the duration of events. Some characteristics are added such as; dominant type of each event (colors dots) , the detection of events by both instruments (black asterisk) versus the detection only by the PARSIVEL2(black dot) and the number of intense occurrences (extracted from total events 129) is labeled on the yellow-marked locations.

To illustrate the overestimation mechanism, we examine an extreme event recorded on March 17, 2023 (event number 80, Fig. 10). During this 4.5-hour event (09:29–15:24 LT), the PARSIVEL^2 accumulated 47.9 mm compared to only 8.2 mm measured by the Pluvio^2, yielding an overestimation of 458%. The rain intensity time series (Fig. 10a) reveals that the highest intensity peaks reaching up to 0.9 mm/min coincide with minutes classified as soft hail and hail, while snow, rain, and drizzle periods exhibit substantially lower intensities. The particle size distributions during these high intensity periods (Fig. 10c) show that large particles exceeding 10 mm, classified as hail,coexist simultaneously with a high concentration of smaller particles below 5 mm belonging to other hydrometeor types. The PARSIVEL^2 algorithm attributes all detected particles within each sampling minute to the total precipitation amount, irrespective of classification ambiguities, which directly drives the observed overestimation.

The Pluvio^2 response (red line, Fig. 10a) contrasts markedly with the PARSIVEL^2 signal, evidencing the fundamental difference in detection principles between the two instruments. The weighing gauge requires sufficient mass accumulation to exceed its detection threshold, resulting in an approximate one hour delay before registration begins. Moreover, the Pluvio^2 record exhibits a distinctive oscillatory pattern: intensity rises to a local peak, decreases toward near zero values, and subsequently recovers with a new peak. This behavior reflects the instrument's limited sensitivity to intermittent precipitation, as mass accumulation is interrupted when precipitation temporarily ceases or falls below the detection threshold. A limitation particularly relevant in high altitude transition zones where precipitation arrives in discontinuous pulses driven by moisture fluxes advected from the Amazon basin toward the Andes.

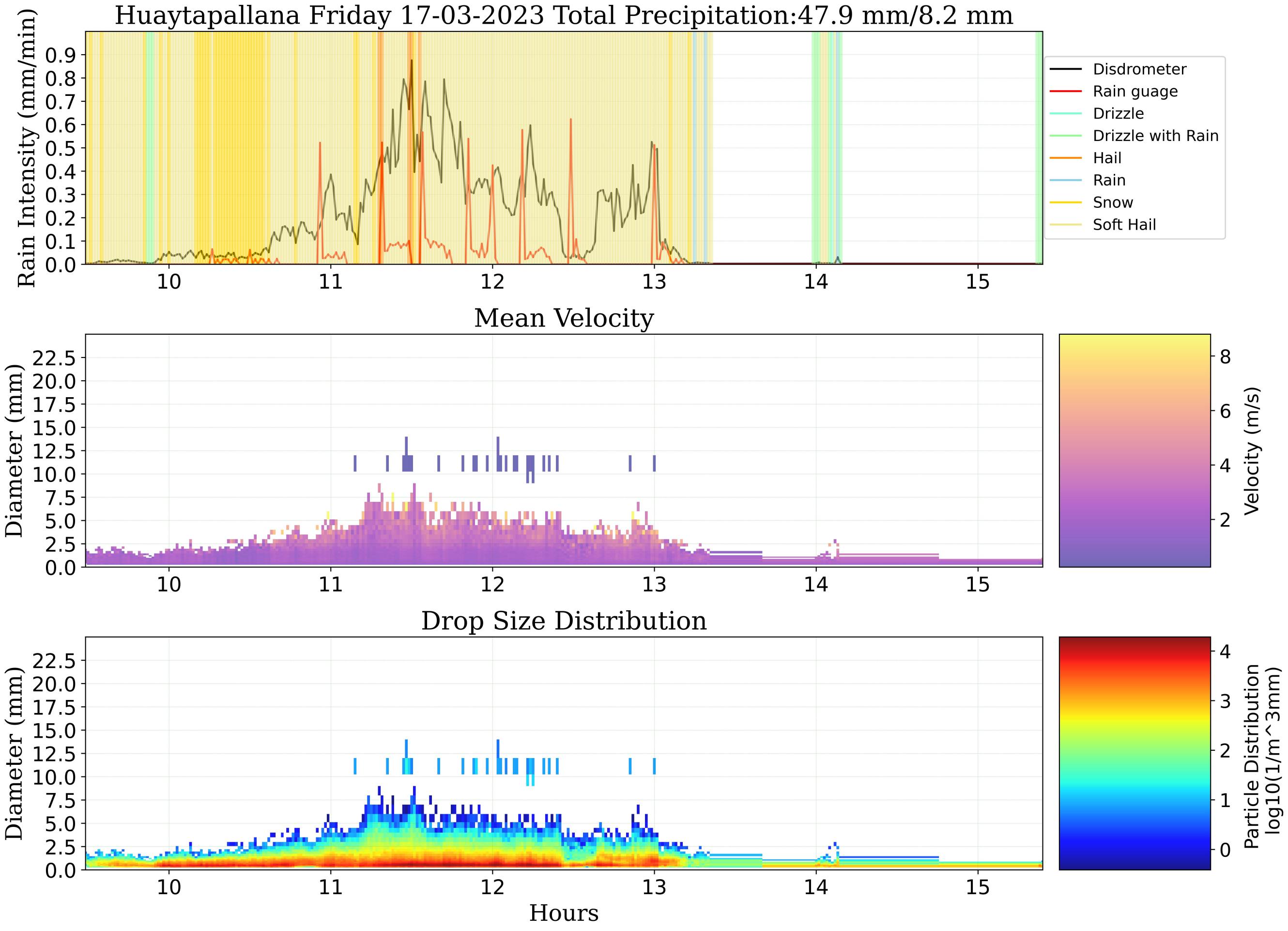

Figure 10. Case study of extreme overestimation event (80: March 17, 2023): (a) precipitation intensity time series colored by classified hydrometeor type; (b) the behavior of mean fall velocity variable according diameter sizes during the event; (c) particle size distributions during the event, showing coexistence of multiple size particles.

This oscillatory pattern can be further interpreted through the microphysical observations. The mean velocity panel (Fig. 10b) shows that the decreasing phases of the Pluvio^2 signal are associated with higher mean fall velocities at small diameters (below 2.5 mm), suggesting a dominance of fast falling, high-concentration small particles, likely soft hail or graupel, that may bounce or partially shed off the weighing funnel rather than contributing fully to the accumulated mass. Conversely, elongated particles with diameters around 7.5 mm appear at low concentrations and higher velocities, consistent with hailstone passages. The particle size distribution (Fig. 10c) corroborates this interpretation, showing that peak concentration episodes are dominated by small particles with high number densities,while the large diameter tail reflects sporadic but optically significant hail detections that disproportionately inflate the PARSIVEL^2 accumulation.

The extreme overestimation observed across these cases exceeding 83% for solid precipitation and 98% for mixed events is driven by a combination of large particles with high terminal velocities (~ 8 m s^{-1}), high particle concentrations, and the coexistence of multiple hydrometeor types within the same sampling interval. These results confirm that when the instrument's minute-averaged classification fails, errors propagate exponentially due to the D^3 dependence in volume flux calculations. This systematic bias identified at the event scale demonstrates that uncorrected optical disdrometer data are unsuitable for climatological applications in high-mountain tropical settings. Consequently, the magnitude of these errors necessitates a post-processing correction, as presented and validated in the following section through a hydrometeor-specific density adjustment algorithm.

4.3 Application and Results of the Correction Method

After applying segmentation based on empirical curves derived from the velocity-diameter relationship to each minute of raw disdrometer data, the new classification revealed significant changes over the study period (Fig. 11). Rain remained the dominant hydrometeor type, accounting for 52% of all precipitation. However, wet snow emerged as the second most abundant type (29.3%), followed by graupel (15%). Pure snow events decreased drastically from the initial classification (approximately 26%) to only 3.7% after applying the correction methodology. Soft hail represented 0.0% in the final classification. When categorized by phase, liquid precipitation comprised 52%, mixed-phase precipitation accounted for 29.3%, and solid precipitation represented 18.7% of the total.

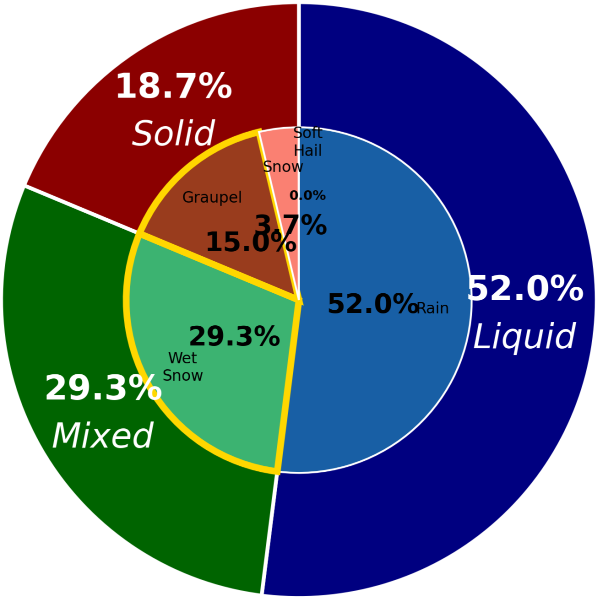

Figure 11. New classification of hydrometeor types after correction method applied. The inner pie chart shows the percentages of each types highlighting wet snow and graupel as the newly emerged dominant solid phase categories. These types are grouped into liquid, solid, and mixed phases in the outer pie chart

4.3.1 Apparent density calculation

Before calculating the apparent density, it is worth noting that the PARSIVEL^2 internally computes a density value for each classified minute, which should follow the empirical diameter density relationship proposed by Brandes et al. (2008). However, analysis of these internal values revealed systematic deviations from theoretical expectations across all precipitation phases (Fig. 12). Solid particles showed median densities near 0.48 g cm^{-3} with high variability (0.02–1.7 g cm^{-3}); liquid particles clustered around 0.93 g cm^{-3} with a narrow interquartile range, though outliers extended from 0.08 to 1.9 g cm^{-3}; and mixed-phase particles presented intermediate values (median 0.87 g cm^{-3}) with moderate variability. These deviations confirm that the disdrometer's internal algorithm does not reliably reproduce standard theoretical density values, underscoring the need for site specific calibration.

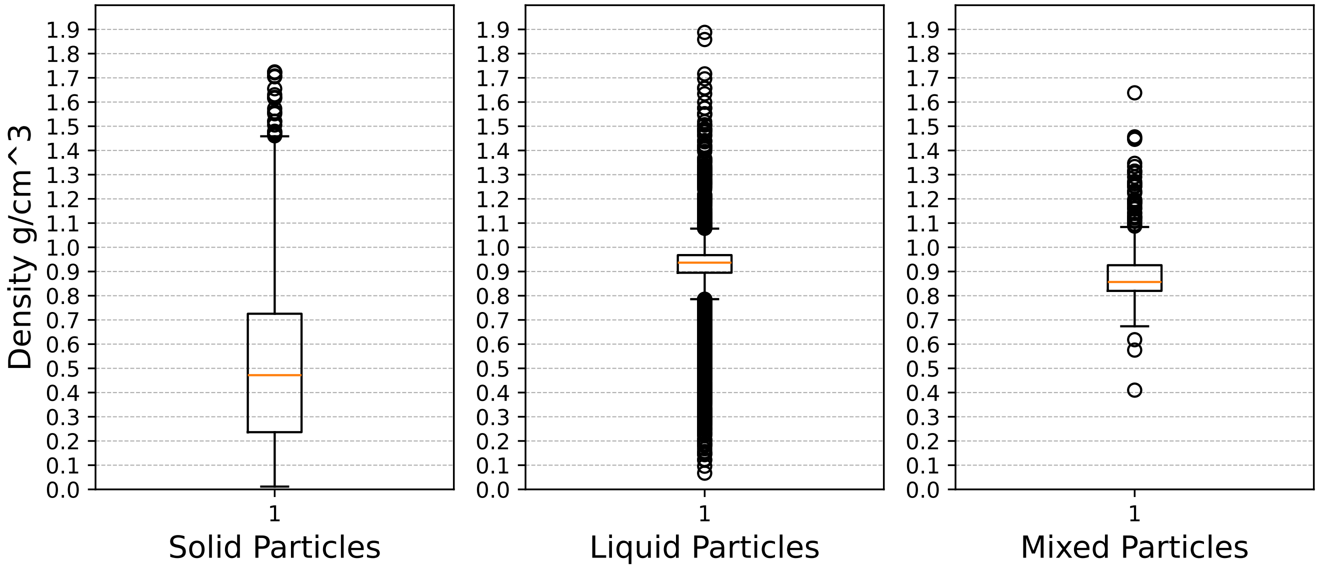

Figure 12. Distribution of density value in box plot grouped by each phase type. The density value shows ranging from 0 to 1.90 g/cm3 , the orange line represents the 50th percentile and the black circles are outlier values.

Table 3. Density values of hydrometeor categories: Theoretical range and best fitting value calculation

Hydrometeor Category	Density Range	Apparent Density
Rain	0.9–1.0	0.90
Snow	0.05–0.35	0.05
Wet Snow	0.1–0.2	0.10
Graupel	0.05–0.45	0.06
Hailstones	0.31–0.61	0.31

In addition to segmenting the disdrometer raw data by hydrometeor category, we estimated bulk density using observations from the weighing rain gauge. Apparent densities estimated from the optimization procedure (Table 3) fell within the theoretical ranges for each hydrometeor category. Rain exhibited an apparent density of 0.9 g cm^{-3}, close to the theoretical upper limit for liquid water. Solid precipitation types showed considerably lower values: snow (0.05 g cm^{-3}), wet snow (0.10 g cm^{-3}), graupel (0.06 g cm^{-3}), and hailstones (0.31 g cm^{-3}), all within expected ranges but toward their lower bounds, consistent with the porous structure of solid hydrometeors at high altitude sites.

4.3.2 Corrected precipitation totals

The application of hydrometeor specific density corrections produced markedly different outcomes depending on the precipitation phase regime (Fig. 13). The largest improvement was observed for mixed precipitation, where systematic overestimation decreased from +98.5% to +52.1% and the regression slope converged from 1.936 to 1.004, with RMSE reduced from 7.60

to 2.39 mm. Liquid and solid precipitation, in contrast, shifted from overestimation to slight underestimation after correction: liquid events showed a bias of -4.9% (slope 0.743), while solid events transitioned from +84.1% overestimation to -14.1% underestimation (slope 0.779), with RMSE improving from 13.05 to 4.44 mm. The phase dependent behaviour of the correction is examined below through the regression line analysis for each group.

For liquid precipitation (Fig. 13d), the regression line crossed the 1:1 reference at approximately 0.743 mm. Below this threshold, the positive intercept (+0.199 mm) produced marginal overestimation; above it, the sub unity slope (0.743) yielded progressive underestimation reaching approximately -1.1 mm at 5 mm of reference accumulation. The modest increase in RMSE (0.71 → 0.86 mm) and MAE (0.40 → 0.50 mm) reflects the physical constraints of applying a fixed density value to a particle population whose effective density varies at the sub event scale. At this high altitude site, liquid precipitation frequently includes small non spherical particles, drizzle and supercooled droplets, whose effective density deviates marginally from unity due to shape deformation and partial freezing in sub zero ambient air, as evidenced by the outliers in Fig. 12. A time varying density would capture this variability more precisely but would introduce poorly constrained uncertainty; the fixed value of 0.9 g cm^{-3} represents a deliberate trade off that prioritises reproducibility over minute scale precision. The resulting underestimation of -4.9% is consistent with previously reported biases for optical disdrometers at high altitude sites (Valdivia et al., 2020).

For solid precipitation (Fig. 13e), the correction substantially reduced the pre existing overestimation, with RMSE decreasing from 13.05 to 4.44 mm and bias shifting from +84.1% to -14.1%. The regression line crossed the 1:1 reference at approximately 3.8 mm: below this point the positive intercept (+0.887 mm) produced slight overestimation, while above it the sub unity slope (0.779) yielded progressive underestimation reaching approximately -3.7 mm at 20 mm of reference accumulation. This residual underestimation may reflect limitations in the assigned apparent density for intense solid events, where wet snow or rimed hydrometeors could exhibit densities above the correction value. Two extreme events (26 and 80) remained as notable outliers and exerted disproportionate influence on the regression fit, contributing to the comparatively low R^2 (69.12%) despite the marked improvement in absolute error metrics. Following correction and reclassification, no event retained a purely solid hydrometeor composition, all previously solid events were found to contain a measurable liquid or wet snow fraction, suggesting that the uncorrected PARSIVEL^2 systematically misclassified mixed-phase hydrometeors under the atmospheric conditions of this site.

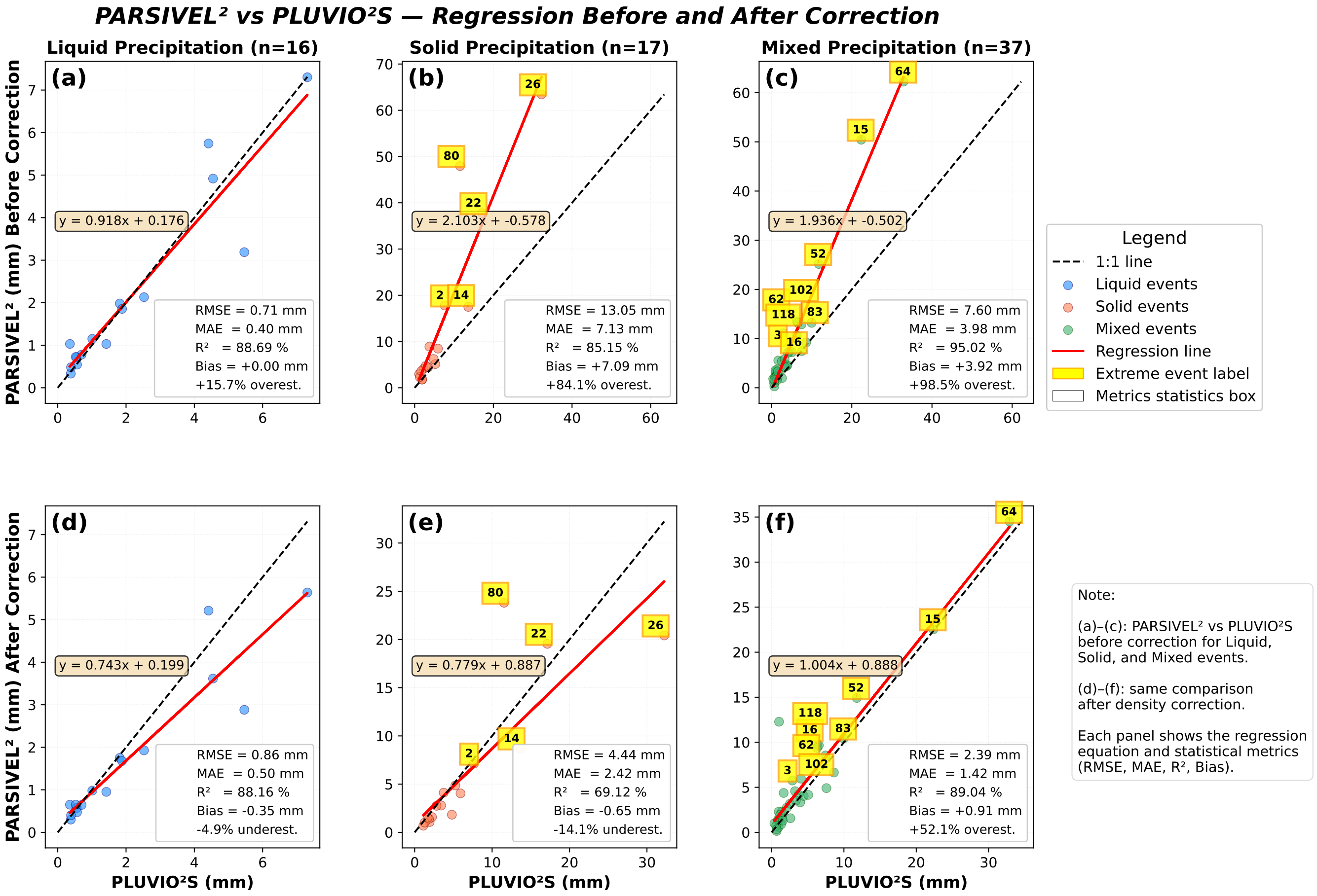

Figure 13. Scatter plots comparing precipitation accumulation measured by the PARSIVEL^2 optical disdrometer with that measured by the reference PLUVIO^{2}S weighing gauge, before (panels a–c) and after (panels d–f) density correction, for three hydrometeor phase categories: liquid precipitation (a, d; $n = 16$), solid precipitation (b, e; $n = 17$), and mixed precipitation (c, f; $n = 37$). Event classification is based on the uncorrected PARSIVEL^2 phase output, using a threshold of >80% fractional contribution of snow, soft hail, and hail for solid events and >80% rain for liquid events. Each panel includes the ordinary least-squares regression equation, the 1:1 reference line (dashed), and key performance metrics: root mean square error (RMSE), mean absolute error (MAE), coefficient of determination (R^2), and systematic bias (mm and percentage overestimation or underestimation). Yellow labels identify individual events with accumulations exceeding 10.6 mm, which disproportionately influence the regression statistics. The density correction substantially reduced the systematic overestimation for solid and mixed events, whereas performance for liquid events remained largely unchanged, consistent with the near-constant density of rainwater ($0.9\,\mathrm{g\,cm^{-3}}$).

Mixed precipitation events (Fig. 13f) showed the strongest response to the density correction among all phase categories. With a regression slope of 1.004 and RMSE reduced from 7.60 to 2.39 mm, this category achieved the closest agreement with the PLUVIO^{2}S reference across the full accumulation range. The regression line remained consistently above the 1:1 reference throughout the observed range, driven by the positive intercept (+0.888 mm). This offset was most pronounced for 485

https://doi.org/10.5194/egusphere-2026-2705
Preprint. Discussion started: 8 July 2026

low-accumulation events and diminished progressively with increasing depth: at 30 mm of reference accumulation, the residual overestimation fell below 0.7 mm, rendering the corrected PARSIVEL^2 essentially equivalent to the reference gauge for moderate to intense events. The elevated percentage bias (+52.1%) reflects the predominance of low accumulation events in this category — most mixed events recorded less than 3 mm, a range in which the near constant intercept offset represents a large relative fraction of the total accumulation. The near unity slope and the substantial RMSE reduction collectively demonstrate that the category specific density correction is most effective precisely where phase complexity is greatest, resolving the error that a single fixed density factor cannot capture.

The impact of the integrated correction on the most intense events of the record is examined in the following subsection.

4.4 Integrated correction impact on extreme precipitation events

Figure 14 shows the particle size distributions (PSDs) before (a) and after (b) applying the complete correction methodology for the 14 most intense events (total precipitation $>$10.6 mm), comprising solid and mixed precipitation. Comparing both panels reveals the selective nature of the integrated correction: the filtering procedure acted on the large diameter tail of the distributions while leaving the physically coherent small tomoderate diameter range largely intact.

Prior to correction (Fig. 14a), several PSDs exhibited discontinuities in the large diameter range; number concentrations declined steeply with increasing diameter but reappeared at isolated bins beyond 10 mm, with some events showing detections above 19 mm. This non monotonic behaviour is physically inconsistent with natural precipitation processes, as it implies the presence of particles whose size velocity relationship deviates from established fall speed curves for any known hydrometeor type (Atlas et al., 1973; Gunn and Kinzer, 1949), suggesting that these detections correspond to contaminating particles rather than precipitation. Uncorrected event totals ranged from 10.64 to 63.44 mm, with the highest accumulations driven by the combined effect of these spurious large diameter detections and the density values calculated by the instrument's internal algorithm, which were shown to deviate systematically from theoretical expectations (Section 4.1).

After implementing the integrated correction (Fig. 14b), the spurious large diameter detections were removed by the velocity–diameter quality control, while number concentrations across small and moderate diameter classes were preserved, confirming that the procedure selectively eliminated contaminating particles without distorting the bulk of the detected hydrometeor population. The corrected PSDs are unimodal, with modal sizes consistently between 0.5 and 2.5 mm across all 14 events, reflecting the microphysical characteristics of precipitation at this high-altitude site where mixed-phase events predominate. Corrected event totals decreased by 9%–68% relative to uncorrected values. Representative reductions include Event 26 (63.44 $\rightarrow$ 20.42 mm; $-$68%), Event 15 (50.44 $\rightarrow$ 22.54 mm; $-$55%), Event 64 (62.25 $\rightarrow$ 34.51 mm; $-$45%), and Event 2 (17.80 $\rightarrow$ 7.12 mm; $-$60%).

The magnitude of these reductions confirms that the pre correction overestimation documented in Section 4.3 arose from multiple interacting error sources; the misclassification of mixed-phase hydrometeors as purely solid, the inclusion of physically implausible large diameter particles, and the systematic deviation of the instrument's internally calculated density values from theoretical expectations. The integrated correction methodology addressed each of these sources independently, yielding PSDs and accumulation totals that are physically consistent with the precipitation regimes observed at this site. The unimodal structure and the modal diameter range obtained after correction constitute an observational characterisation of extreme precipitation microphysics at this high-altitude location, contributing to the limited body of knowledge on hydrometeor size distributions in tropical glacier environments.

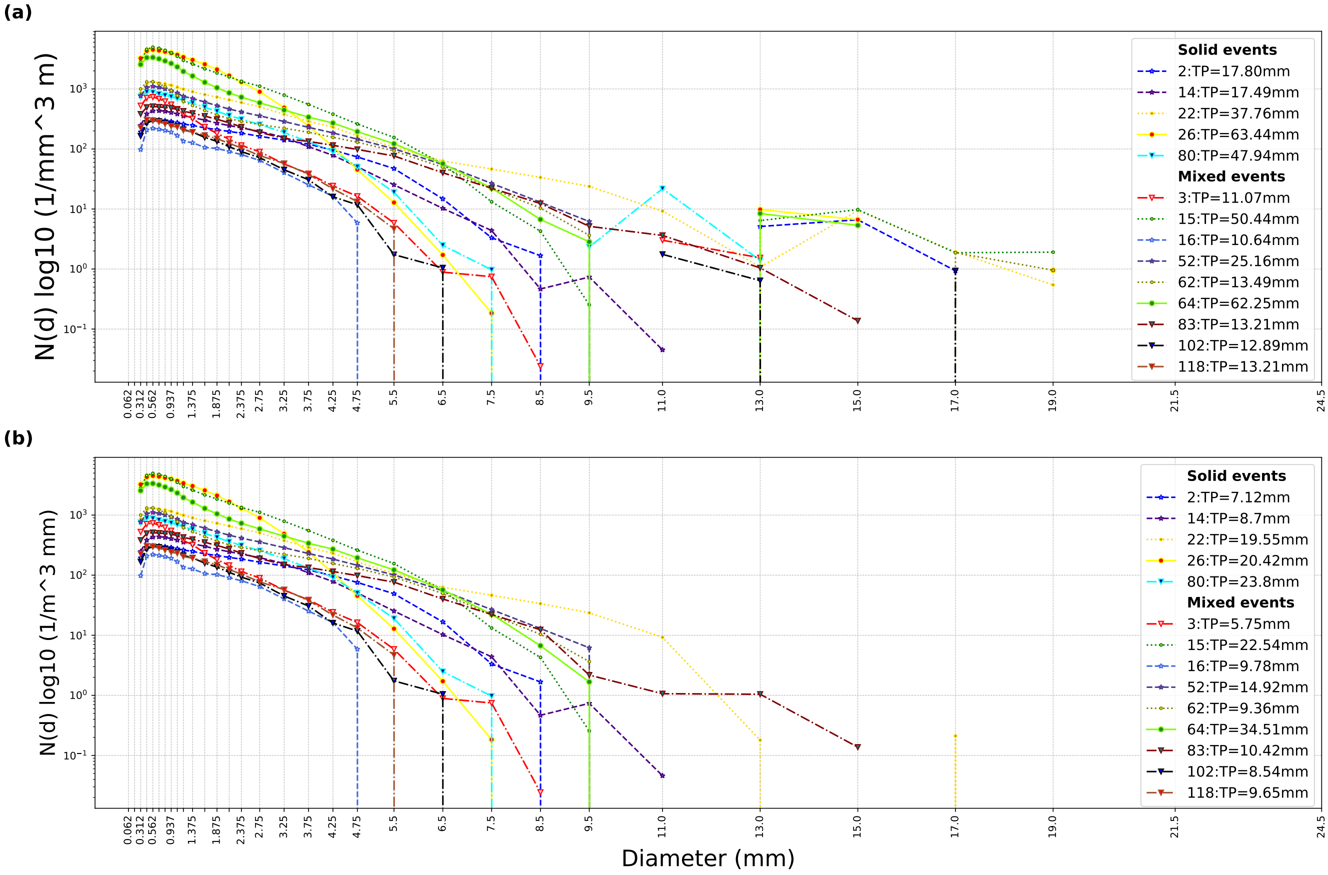

Figure 14. The particle size distribution of extreme events before correction (a), and after correction (b). Each color represents the behavior of particles concentration of a event from the 14 extreme events identified, while increasing the diameter the concentration decrease. The spurious particles in higher diameter and low velocity are cleaned.

5 Discussion

5.1 Hydrometeor characterization and physical implications

Using the correction method based on empirical velocity-diameter curves, we found a substantial redistribution of precipitation types: wet snow (29.3%) and graupel (15.0%) emerged as dominant categories, whereas pure snow accounted for only 3.7%. Although these types were not validated with direct observations or particle imaging instruments, this work provides a first detailed characterization of hydrometeor types at a tropical glacier in the central Andes, offering an initial basis for understanding precipitation processes in these understudied environments.

The predominance of mixed-phase precipitation over pure snowfall is consistent with the thermodynamic structure of tropical glacier environments, where the freezing level often oscillates near the surface and temperatures rarely remain sufficiently low for long periods to sustain exclusively solid precipitation (Sicart et al., 2005; Favier et al., 2004). At our site (4709 m a.s.l.), temperatures during precipitation events ranged from -1.6 to 9.2°C, favoring phase coexistence and partial melting during particle fall.

The identification of wet snow as the dominant hydrometeor has direct implications for the glacier radiative balance and melting dynamics. Wet snow typically exhibits lower albedo (0.5–0.7) than fresh dry snow (0.8–0.9) due to larger grain size and liquid-water content, increasing shortwave absorption and accelerating melt (Wiscombe and Warren, 1980; Melloh et al., 2002). In addition, its higher density (0.1–$0.2\,\mathrm{g\,cm^{-3}}$ versus 0.04–$0.1\,\mathrm{g\,cm^{-3}}$ for dry snow) influences snowpack metamorphism and water percolation, potentially leading to earlier and faster contributions to glacier runoff (Cuffey and Paterson, 2010). Graupel, owing to its compact structure and relatively high density, can also melt more rapidly than snow crystals after deposition on the glacier surface.Furthermore, the event integrated PSDs of the 14 most intense events revealed a consistent unimodal structure with modal diameters between 0.5 and 2.5 mm, suggesting that this size range characterises the bulk of the hydrometeor population at this site regardless of event intensity.A finding that may inform parameterisation schemes for microphysical modelling in similar high-altitude tropical environments.

Future studies should incorporate direct observation instruments to validate the hydrometeor classification inferred from the velocity–diameter method. Multi-Angle Snowflake Cameras (MASC; (Garrett et al., 2012)) or other particle-imaging systems (Praz et al., 2017) could provide detailed morphological information to confirm the identified types and quantify riming and crystal habits. In addition, vertically pointing cloud radars (e.g., Micro Rain Radar) would enable investigation of the vertical structure of precipitation and the melting-level height, supporting a process-level understanding of mixed-phase precipitation formation mechanisms in this tropical orographic environment (Mace et al., 2009).

5.2 Transfer function performance and limitations

To correct the underestimation of the Pluvio2 weighing gauge due to the lack of wind shielding, we applied the transfer function proposed by Kochendorfer et al. (2017), which adjusts accumulation as a function of wind speed and temperature. The correction increased the raw measurements by 14% on average. The method uses empirical coefficients derived from the WMO Solid Precipitation Intercomparison Experiment (WMO-SPICE) and has been evaluated across diverse climatic conditions.

The meteorological conditions at our site fall within the validity ranges reported by Kochendorfer et al. (2017). Selected precipitation events occurred at temperatures between -0.45 and $4.85\,^{\circ}\mathrm{C}$ (critical threshold: $< -2\,^{\circ}\mathrm{C}$) and wind speeds between 0.7 and $5.48\,\mathrm{m\,s^{-1}}$ (critical threshold: $> 7.2\,\mathrm{m\,s^{-1}}$), reducing the uncertainty associated with extrapolation beyond the calibration range. In addition, the average catch efficiency (CE) was 0.85 and did not exceed the physical maximum of 1.0, supporting the applicability of the method in this tropical high-mountain environment.

https://doi.org/10.5194/egusphere-2026-2705
Preprint. Discussion started: 8 July 2026

Despite its effectiveness under appropriate conditions, the method has limitations noted in subsequent studies. Smith et al. (2020) showed that transfer function performance can deteriorate at sites with extreme wind speeds ($> 10\,\mathrm{m\,s^{-1}}$) or in complex mountainous terrain where local aerodynamics can cause non uniform particle capture. At our site, the maximum recorded wind speed (5.48 $\mathrm{m\,s^{-1}}$) reduces this concern; however, the topographic complexity of the periglacial setting (strong local elevation gradients) likely introduces additional uncertainty that is not quantified here. Another limitation is the inability to correct events with zero recorded accumulation; with our event selection threshold ($\geq$0.25 mm), 44 potential events were discarded, representing about 34% of the events detected by PARSIVEL2 but not by Pluvio2. This loss reflects both the limitations of the weighing gauge and the high sensitivity of the disdrometer to very light precipitation that may not be hydrologically significant.

The influence of complex mountainous terrain on Pluvio2 catch efficiency requires further investigation, for example through controlled experiments with multiple spatially distributed sensors or via CFD (computational fluid dynamics) simulations of wind flow around the instrument. In addition, installing a Double Fence Intercomparison Reference (DFIR) would enable direct quantification of wind bias without relying on empirical transfer functions, providing a more robust reference for future calibrations (by BE Goodison et al., 1998).

6 Conclusion

This study evaluated the performance of the PARSIVEL^{2}OTT optical disdrometer under tropical glacier conditions at 4709 m a.s.l., an environment characterized by mixed-phase precipitation. The analysis revealed critical limitations in the instrument's ability to distinguish precipitation types that coexist within the same time interval, leading to erroneous classifications that propagate into derived variables. In particular, systematic overestimations exceeding 98% were identified in mixed-phase events, mainly due to the misidentification of large, low density hydrometeors (e.g., wet snow or melting graupel) as high velocity liquid drops. This error is amplified by the D^3 dependence in precipitation intensity calculations, whereby small differences in diameter can produce large errors in accumulated precipitation. These findings show that standard PARSIVEL^2 algorithms are inadequate for tropical glacier environments without post processing corrections.

The correction methodology developed here integrates (1) hydrometeor reclassification using empirical velocity–diameter curves and (2) optimization of type specific apparent densities. Overall, it reduced errors in extreme events by up to 68%. The largest improvement was obtained for mixed-phase precipitation, where the regression slope improved from 1.936 (almost double the reference) to 1.004 (near ideal), and the RMSE decreased from 7.60 to 2.39 mm. The corrected classification yielded a more physically plausible hydrometeor type distribution: pure snow decreased from 26% to 3.7%, whereas wet snow (29.3%) and graupel (15.0%) emerged as the dominant solid hydrometeors. This result has direct implications for glacier mass balance assessments, as wet snow exhibits lower albedo and higher density than dry snow, accelerating shortwave energy absorption and modifying snowpack metamorphism rates in ways that are not captured when precipitation is misclassified as pure snow. Although the method produces slight underestimations for pure liquid (-4.9%) and solid precipitation (-14.1%), these deviations are acceptable because (a) such events represent a small fraction of the annual total, (b) absolute errors are low (RMSE $< 5\,\mathrm{mm}$), and (c) correcting mixed-phase events (more than 50% of cases) is critical for reliable hydrological estimates.

This article provides a validated post processing methodology for optical disdrometers in tropical glacial environments, where mixed-phase precipitation dominates the hydrological regime. Accurate quantification of solid versus liquid precipitation is essential for glacier mass balance studies and for accumulation and ablation models that project andean glacier evolution under climate change. Improved precipitation estimates also support water resources management by strengthening predictions of seasonal water availability for agriculture, domestic use, and hydropower generation. Finally, the refined precipitation-type characterization (with wet snow and graupel identified as prevalent hydrometeors) contributes to the understanding of microphysical cloud processes in the tropical upper troposphere, which remains understudied.

The methodology is limited by its reliance on a calibrated weighing rain gauge as reference and by the lack of direct validation of hydrometeor morphology. Although direct observation instruments (e.g., 2DVD cameras or particle imaging systems) would improve validation, their cost and operational complexity limit their use in extensive monitoring networks. A key advantage of the proposed approach is that it can be implemented within existing automated station networks without additional instrumentation, reducing costs and improving the reliability of precipitation data in remote high mountain areas. This supports transferability to other high elevation tropical glacier sites in the Andes (Peru, Ecuador, Bolivia, Colombia) operating under similar thermal conditions. Future work should (a) validate the method with direct observations or particle imaging, (b) extend the analysis to multiple years to assess ENSO related interannual variability, and (c) integrate corrected precipitation into distributed glacier mass balance models to improve projections of glacier retreat under future climate scenarios.

Code and data availability.

The data used in this work can be acquired downloaded from the repository (OTT PARSIVEL2, AWS and OTT PLUVIO2S records — Cordillera Huaytapallana, Peru 2022–2023) DOI: https://doi.org/10.5281/zenodo.20756952 Perez (2026b) The script developed for the method applied can be found in https://doi.org/10.5281/zenodo.19808059 Perez (2026a)

Author contributions.

MAP, JMV and YSP conceptualized the study. EVP and YSV provided the resources. MAP and JMV conducted the formal analysis and design the methodology. MAP developed the software and visualization. IP and YSV secured the funding, administered the project and supervised the project. MAP, IP, JMV,DM and EVP validated the results. MAP wrote the original draft of the manuscript. MAP, JMV and DM and reviewed and edited the manuscript.

Competing interests. The authors declare that they have no competing interests.

Acknowledgements. Special thanks to Dr. José Luis Flores Rojas for his support and feedback during the research presentations, and to Meteorological Engineer Jared Zuñiga Human for his guidance in programming during the early stages of this investigation. This work is part of a thesis research developed at the Universidad Continental (Huancayo, Peru), with institutional support from the Instituto Geofísico del Perú (IGP). The input dataset used in this paper was collected within the framework of the TAMYA Project: "Impactos de la precipitación, registrados con un radar meteorológico, en los cuerpos glaciares Andinos: Nevado Huaytapallana", funded by CONCYTEC – FONDECYT, Grant No. 082-2021-FONDECYT, in collaboration with IMAGEM (Instituto Nacional de Investigación en Glaciares y Ecosistemas de Montaña) and IGP. The TAMYA Project provided the observational infrastructure and raw data used in this study but did not fund the thesis or its publication directly. We acknowledge the assistance of Anthropic's Claude, an artificial intelligence language model, in refining the language structure and improving the clarity of this manuscript. All scientific interpretations, analyses, and conclusions remain entirely the responsibility of the authors.

References

Allen, J. T., Giammanco, I. M., Kumjian, M. R., Punge, H. J., Zhang, Q., Groenemeijer, P., Kunz, M., and Ortega, K.: Understanding Hail in the Earth System, https://doi.org/10.1029/2019RG000665, 2020.

Annella, C., Capozzi, V., Fusco, G., Budillon, G., and Montopoli, M.: Error investigation of rain retrievals from disdrometer data using triple colocation, Atmospheric Science Letters, 23, https://doi.org/10.1002/asl.1127, seria muy interesante hacer al intercomparación con este metodo de triple colocación entre el rain gauge, weighing rain gauge, parsivel. Just to validate pluvio2., 2022.

Atlas, D., Srivastava, R. C., and Sekhon, R. S.: Doppler Radar Characteristics of Precipitation at Vertical Incidence, Tech. rep., 1973.

Battaglia, A., Rustemeier, E., Tokay, A., Blahak, U., and Simmer, C.: PARSIVEL snow observations: A critical assessment, Journal of Atmospheric and Oceanic Technology, 27, 333–344, https://doi.org/10.1175/2009JTECHA1332.1, 2010.

Boudala, F. S., Isaac, G. A., Rasmussen, R., Cober, S. G., and Scott, B.: Comparisons of Snowfall Measurements in Complex Terrain Made During the 2010 Winter Olympics in Vancouver, Pure and Applied Geophysics, 171, 113–127, https://doi.org/10.1007/s00024-012-0610-5, 2014.

Brandes, E. A., Ikeda, K., Thompson, G., and Schönhuber, M.: Aggregate terminal velocity/temperature relations, Journal of Applied Meteorology and Climatology, 47, 2729–2736, https://doi.org/10.1175/2008JAMC1869.1, 2008.

Bringi, V., Thurai, M., and Baumgardner, D.: Raindrop fall velocities from an optical array probe and 2-D video disdrometer, Atmospheric Measurement Techniques, 11, 1377–1384, https://doi.org/10.5194/amt-11-1377-2018, 2018.

Buytaert, W., Moulds, S., Acosta, L., Bièvre, B. D., Olmos, C., Villacis, M., Tovar, C., and Verbist, K. M.: Glacial melt content of water use in the tropical Andes, Environmental Research Letters, 12, https://doi.org/10.1088/1748-9326/aa926c, 2017.

by BE Goodison, Louie, P., and Yang, D.: WMO SOLID PRECIPITATION MEASUREMENT INTERCOMPARISON FINAL REPORT, Tech. rep., World Meteorological Organization, 1998.

C., K. N. and J., H. A.: Measurement and Interpretation of Hailstone Density and Terminal Velocity, Journal of Applied Meteorology, 40, 1510–1516, 1983.

Cadeddu, M. P., Ghate, V. P., and Mech, M.: Ground-based observations of cloud and drizzle liquid water path in stratocumulus clouds, Atmospheric Measurement Techniques, 13, 1485–1499, https://doi.org/10.5194/amt-13-1485-2020, 2020.

Colli, M., Lanza, L. G., and Barbera, P. L.: The performance of weighing gauges under laboratory simulated severe real world precipitation events, Tech. rep., 2013.

Cuffey, K. and Paterson, W.: The physics of glaciers, Journal of Glaciology, 57, 383–384, https://doi.org/10.3189/002214311796405906, 2010.

Dadic, R., Mott, R., Lehning, M., Carenzo, M., Anderson, B., and Mackintosh, A.: Sensitivity of turbulent fluxes to wind speed over snow surfaces in different climatic settings, Advances in Water Resources, 55, 178–189, https://doi.org/10.1016/j.advwatres.2012.06.010, in general, they analysis the impact of wind speed over snow surface. Finding, the heat flux interacction with other vaiables like huminity, air temprature change with high wind speed, which increase reduction of snow cover. Also they mention about sheldered sites with low wind speed, aht means good and portected are, and the future form small glaciers., 2013.

Espinoza, J. C., Garreaud, R., Poveda, G., Arias, P. A., Molina-Carpio, J., Masiokas, M., Viale, M., and Scaff, L.: Hydroclimate of the Andes Part I: Main Climatic Features, https://doi.org/10.3389/feart.2020.00064, 2020.

Favier, V., Wagnon, P., and Ribstein, P.: Glaciers of the outer and inner tropics: A different behaviour but a common response to climatic forcing, Geophysical Research Letters, 31, https://doi.org/10.1029/2004GL020654, 2004.

Fehlmann, M., Rohrer, M., Lerber, A. V., and Stoffel, M.: Automated precipitation monitoring with the Thies disdrometer: Biases and ways for improvement, Atmospheric Measurement Techniques, 13, 4683–4698, https://doi.org/10.5194/amt-13-4683-2020, 2020.

Footec, G. B. and Toit, P. S. D.: Terminal Velocity of Raindrops Aloft, Journal of Applied Meteorology and Climatology, pp. 249–253, el calculo de la velocidad terminar a otro nivel que no sea a nivel del mal es discutido. La atencion esta llamada a la medicion atual de la velocidad termianl a diferentes densidades de aire., 1969.

Fuchs', T., Rapp', J., Rubep, F., and Rudolf', B.: Correction of Synoptic Precipitation Observations due to Systematic Measuring Errors with Special Regard to Precipitation Phases, Tech. rep., 2001.

Garrett, T. J., Fallgatter, C., Shkurko, K., and Howlett, D.: Fall Speed Measurement and High-Resolution Multi-Angle Photography of Hydrometeors in Free Fall, Atmospheric Measurement Techniques, 5, 2625–2633, https://doi.org/10.5194/amt-5-2625-2012, 2012.

Grazioli, J., Genthon, C., Boudevillain, B., Duran-Alarcon, C., Guasta, M. D., Madeleine, J. B., and Berne, A.: Measurements of precipitation in Dumont d'Urville, Adélie Land, East Antarctica, Cryosphere, 11, 1797–1811, https://doi.org/10.5194/tc-11-1797-2017, 2017.

Gualco, L. F., Campozano, L., Maisincho, L., Robaina, L., Muñoz, L., Ruiz-Hernández, J. C., Villacís, M., and Condom, T.: Corrections of precipitation particle size distribution measured by a parsivel OTT2 disdrometer under windy conditions in the antisana massif, Ecuador, Water (Switzerland), 13, https://doi.org/10.3390/w13182576, 2021.

Gunn, R. and Kinzer, G. D.: THE TERMINAL VELOCITY OF FALL FOR WATER DROPLETS IN STAGNANT AIR, Journal of the Atmospheric Sciences, pp. 243–248, 1949.

Heymsfield, A. and Wright, R.: Graupel and hail terminal velocities: Does a "Supercritical" Reynolds number apply?, Journal of the Atmospheric Sciences, 71, 3392–3403, https://doi.org/10.1175/JAS-D-14-0034.1, 2014.

Hobbs, P. V. and Rangno, A. L.: Super-large raindrops, Geophysical Research Letters, 31, https://doi.org/10.1029/2004GL020167, 2004.

Hobbs, P. V., Chang, S., and Locatelli, J. D.: The dimensions and aggregation of ice crystals in natural clouds, Journal of Geophysical Research, 79, 2199–2206, https://doi.org/10.1029/jc079i015p02199, 1974.

HydroMet, O.: Operating Instructions Precipitation gauge OTT Pluvio2 S, Tech. rep., 2019.

Ishizaka, M., Motoyoshi, H., Nakai, S., Shiina, T., Kumakura, T., and Muramoto, K. I.: A new method for identifying the main type of solid hydrometeors contributing to snowfall from measured size-fall speed relationship, Journal of the Meteorological Society of Japan, 91, 747–762, https://doi.org/10.2151/jmsj.2013-602, 2013.

Jia, Y., Li, Z., Wang, F., and Chen, P.: Correction of precipitation measurement for weighing precipitation gauges in a glacierized basin in the Tianshan Mountains, Frontiers in Earth Science, 11, https://doi.org/10.3389/feart.2023.1115299, 2023.

Kochendorfer, J., Nitu, R., Wolff, M., Mekis, E., Rasmussen, R., Baker, B., Earle, M. E., Reverdin, A., Wong, K., Smith, C. D., Yang, D., Roulet, Y. A., Buisan, S., Laine, T., Lee, G., Aceituno, J. L. C., Alastrué, J., Isaksen, K., Meyers, T., Brækkan, R., Landolt, S., Jachcik, A., and Poikonen, A.: Analysis of single-Alter-shielded and unshielded measurements of mixed and solid precipitation from WMO-SPICE, Hydrology and Earth System Sciences, 21, 3525–3542, https://doi.org/10.5194/hess-21-3525-2017, 2017.

Kochendorfer, J., Nitu, R., Wolff, M., Mekis, E., Rasmussen, R., Baker, B., Earle, M., Reverdin, A., Wong, K., Smith, C. D., Yang, D., Roulet, Y. A., Meyers, T., Buisan, S., Isaksen, K., Brækkan, R., Landolt, S., and Jachcik, A.: Testing and development of transfer functions for weighing precipitation gauges in WMO-SPICE, Hydrology and Earth System Sciences, 22, 1437–1452, https://doi.org/10.5194/hess-22-1437-2018, 2018.

Lawson, R. P., Stewart, R. E., and Angus, L. J.: Observations and Numerical Simulations of the Origin and Development of Very Large Snowflakes, Tech. rep., Journal of the Atmospheric Sciences, https://doi.org/https://doi.org/10.1175/1520-0469(1998)055<3209:OANSOT>2.0.CO;2, 1998.

Licznar, P. and Krajewski, W. F.: Precipitation Type Specific Radar Reflectivity-Rain Rate Relationships for Warsaw, Poland, Acta Geophysica, 64, 1840–1857, https://doi.org/10.1515/acgeo-2016-0071, 2016.

Llactayo, V., Valdivia, J., Yarleque, C., Callañaupa, S., Villalobos-Puma, E., Guizado, D., and Alvarado-Lugo, R.: Future changes of precipitation types in the Peruvian Andes, Scientific Reports, 14, 22 634, https://doi.org/10.1038/s41598-024-71840-2, 2024.

Locatelli, J. D. and Hobbs, P. V.: Fall Speeds and Masses of Solid Precipitation Particles, Tech. rep., 1974.

Löffler, M., Löffler-Mang, M., and Ticinese, O.: An Optical Disdrometer for Measuring Size and Velocity of Hydrometeors, Tech. rep., Journal of Atmospheric and Oceanic Technology, 1999.

Ma, L., Zhao, L., Yang, D., Xiao, Y., Zhang, L., and Qiao, Y.: Analysis of raindrop size distribution characteristics in permafrost regions of the Qinghai-Tibet plateau based on new quality control scheme, Water (Switzerland), 11, https://doi.org/10.3390/w11112265, 2019.

Mace, G. G., Zhang, Q., Vaughan, M., Marchand, R., Stephens, G., Trepte, C., and Winker, D.: A Description of Hydrometeor Layer Occurrence Statistics Derived from the First Year of Merged Cloudsat and CALIPSO Data, Journal of Geophysical Research: Atmospheres, 114, 2007JD009 755, https://doi.org/10.1029/2007JD009755, 2009.

Magono, C. and LEE, C. W.: Meteorological Classification of Natural Snow Crystal, Journal of the Faculty of Science, II, 1966.

Maruyama, K.-I.: Monte Carlo Simulation of the Formation of Snowflakes, Tech. rep., 2005.

Maussion, F., Gurgiser, W., Großhauser, M., Kaser, G., and Marzeion, B.: ENSO influence on surface energy and mass balance at Shallap Glacier, Cordillera Blanca, Peru, Cryosphere, 9, 1663–1683, https://doi.org/10.5194/tc-9-1663-2015, 2015.

Melloh, R. A., Hardy, J. P., Davis, R. E., and Isradar, P. B.: Spectral albedo of snow-covered land; observations and modeling, Hydrological Processes, 16, 2141–2158, https://doi.org/10.1002/hyp.1039, 2002.

Mott, R., Vionnet, V., and Grünewald, T.: The Seasonal Snow Cover Dynamics: Review on Wind-Driven Coupling Processes, https://doi.org/10.3389/feart.2018.00197, paper is really interested if you want to learn more about interaction in small scale with snow and environment features., 2018.

National Snow and Ice Data Center: Science of Snow, https://nsidc.org/learn/parts-cryosphere/snow/science-snow, accessed: 2024-11-28, n.d.

Nemeth, K. and Beck, E.: High-precision measurement of hydrometeors, Meteorological Technology International Magazine, https://www.ott.com/download/meteorological-technology-international-article/, accessed: 2024-08-24, 2011.

Nichols, H. B.: Snow Crystals: Natural and Artificial . Ukichiro Nakaya. Harvard Univ. Press, Cambridge, 1954. xii + 510 pp. Illus. $10, Science, https://api.semanticscholar.org/CorpusID:161610062, 1954.

Perez, M.: Oritiairis/PpTypes_DISDRO_WS: Enabled, https://doi.org/10.5281/zenodo.19808059, 2026a.

Perez, M.: Dataset of PARSIVEL2 disdrometer, GMX500 weather station and PLUVIO2S weighing rain gauge measurements at Tropical Glacier Huaytapallana, Peru (2022–2023), https://doi.org/10.5281/zenodo.20756952, 2026b.

Pollard, W.: Periglacial Processes in Glacial Environments, pp. 537–564, Elsevier Inc., ISBN 9780081005248, https://doi.org/10.1016/B978-0-08-100524-8.00016-6, 2018.

Praz, C., Roulet, Y.-A., and Berne, A.: Solid hydrometeor classification and riming degree estimation from pictures collected with a Multi-Angle Snowflake Camera, Atmospheric Measurement Techniques, 10, 1335–1357, https://doi.org/10.5194/amt-10-1335-2017, 2017.

Ro, Y., Chang, K.-H., Hwang, H., Kim, M., Cha, J.-W., and Lee, C.: Comparative study of rainfall measurement by optical disdrometer, tipping-bucket rain gauge, and weighing precipitation gauge, Natural Hazards, https://doi.org/10.1007/s11069-023-06308-z, 2023.

Shimazaki, A.: Manual on Codes International Codes Volume I.1 Annex II to the WMO Technical Regulations Part A-Alphanumeric Codes 2019 edition, Tech. rep., 2019.

Sicart, J. E., Wagnon, P., and Ribstein, P.: Atmospheric controls of the heat balance of Zongo Glacier (16°S, Bolivia), Journal of Geophysical Research D: Atmospheres, 110, 1–17, https://doi.org/10.1029/2004JD005732, 2005.

Smith, C. D., Ross, A., Kochendorfer, J., Earle, M. E., Wolff, M., Buisán, S., Roulet, Y. A., and Laine, T.: Evaluation of the WMO Solid Precipitation Intercomparison Experiment (SPICE) transfer functions for adjusting the wind bias in solid precipitation measurements, Hydrology and Earth System Sciences, 24, 4025–4043, https://doi.org/10.5194/hess-24-4025-2020, 2020.

Somers, L. D., McKenzie, J. M., Mark, B. G., Lagos, P., Ng, G. H. C., Wickert, A. D., Yarleque, C., Baraër, M., and Silva, Y.: Groundwater Buffers Decreasing Glacier Melt in an Andean Watershed—But Not Forever, Geophysical Research Letters, 46, 13 016–13 026, https://doi.org/10.1029/2019GL084730, 2019.

Straka, J. M.: CLOUD AND PRECIPITATION MICROPHYSICS: Principles and Parameterizations, www.cambridge.org/, 2009.

Szyrmer, W. and Zawadzki, I.: Snow studies. Part II: Average relationship between mass of snowflakes and their terminal fall velocity, Journal of the Atmospheric Sciences, 67, 3319–3335, https://doi.org/10.1175/2010JAS3390.1, 2010.

Thériault, J. M., Leroux, N. R., and Rasmussen, R. M.: Improvement of solid precipitation measurements using a hotplate precipitation gauge, Journal of Hydrometeorology, 22, 877–885, https://doi.org/10.1175/JHM-D-20-0168.1, 2021.

Tokay, A., Wolff, D. B., and Petersen, W. A.: Evaluation of the new version of the laser-optical disdrometer, OTT parsivel, Journal of Atmospheric and Oceanic Technology, 31, 1276–1288, https://doi.org/10.1175/JTECH-D-13-00174.1, 2014.

Tumbusch, M. L.: Evaluation of OTT PLUVIO Precipitation Gage versus Belfort Universal Precipitation Gage 5-780 for the Nation Atmospheric Deposition Program, Tech. rep., 2003.

Valdivia, J. M., Scipión, D. E., Milla, M., and Silva, Y.: Multi-instrument rainfall-rate estimation in the Peruvian central andes, Journal of Atmospheric and Oceanic Technology, 37, 1811–1826, https://doi.org/10.1175/JTECH-D-19-0105.1, 2020.

Valdivia, J. M., Flores-Rojas, J. L., Prado, J. J., Guizado, D., Villalobos-Puma, E., Callañaupa, S., and Silva-Vidal, Y.: Hailstorm events in the Central Andes of Peru: Insights from historical data and radar microphysics, Atmospheric Measurement Techniques, 17, 2295–2316, https://doi.org/10.5194/amt-17-2295-2024, 2024.

Villalobos-Puma, E., Morales, A., Martinez-Castro, D., Valdivia, J., Cardenas-Vigo, R., Lavado-Casimiro, W., and Santiago, A.: Dynamic atmospheric mechanisms associated with the diurnal cycle of hydrometeors and precipitation in the Andes–Amazon transition zone of central Peru during the summer season, Journal of Earth System Science, 133, 75, https://doi.org/10.1007/s12040-024-02278-3, 2024.

Wauben, W. and Pluvio, O.: Precipitation amount and intensity measurements with the Ott Pluvio, Tech. rep., Instrumental Department, INSA-IO, KNMI, 2004.

Wiscombe, W. J. and Warren, S. G.: A Model for the Spectral Albedo of Snow. I: Pure Snow, Journal of the Atmospheric Sciences, 37, 2712–2733, https://doi.org/10.1175/1520-0469(1980)037<2712:AMFTSA>2.0.CO;2, 1980.

Yuter, S. E., Kingsmill, D. E., Nance, L. B., and Löffler-Mang, M.: Observations of Precipitation Size and Fall Speed Characteristics within Coexisting Rain and Wet Snow, Tech. rep., 2006.

Zawadzki, I., Szyrmer, W., Bell, C., and Fabry, F.: Modeling of the Melting Layer. Part III: The Density Effect, Tech. rep., 2005.

Zeng, Y., Yang, L., Tong, Z., Jiang, Y., Zhang, Z., Zhang, J., Zhou, Y., Li, J., Liu, F., and Liu, J.: Statistical Characteristics of Raindrop Size Distribution during Rainy Seasons in Northwest China, Advances in Meteorology, 2021, https://doi.org/10.1155/2021/6667786, 2021.

Zhang, L., Zhao, L., Xie, C., Liu, G., Gao, L., Xiao, Y., Shi, J., and Qiao, Y.: Intercomparison of solid precipitation derived from the weighting rain gauge and optical instruments in the interior Qinghai-Tibetan plateau, Advances in Meteorology, 2015, https://doi.org/10.1155/2015/936724, 2015.

Zikmunda, J. and Vali, G.: Fall Patters and Fall velocities of rimed ice crystals, Journal of Atmospheric Sciences,, 29, 1334–1347, 1972.